Textures, trace elements, and Pb isotopes of sulfides from the Haopinggou vein deposit, southern North China Craton: implications for discrete Au and Ag–Pb–Zn mineralization

Zhan-Ke Li[1] , Jian-Wei Li1,[2] , David R. Cooke[3] , Leonid Danyushevsky[3] , Lejun Zhang[3] , Hugh O'Brien[4] , Yann Lahaye[4] , Wen Zhang[2] , Hai-Jun Xu[5]

1 Faculty of Earth Resources, China University of Geosciences, Wuhan 430074, Hubei Province, China

2 State Key Laboratory of Geological Processes and Mineral Resources, China University of Geosciences, Wuhan 430074, Hubei Province, China

3 Transforming the Mining Value Chain, CODES, University of Tasmania, Private Bag 79, Hobart, TAS 7001, Australia

4 Geological Survey of Finland, P. O. Box 96, 02151 Espoo, Finland

5 Center for Global Tectonics, School of Earth Sciences, China University of Geosciences, Wuhan 430074, Hubei Province, China

Abstract

The Haopinggou deposit in the Xiong'ershan district, southern margin of the North China Craton, comprises numerous Au and Ag–Pb–Zn veins hosted in metamorphic rocks of the Late Archean to early Paleoproterozoic Taihua Group. Two stages of mineralization have been recognized: Stage 1 pyrite–quartz veins and Stage 2 Pb–Zn-sulfide veins. Some pyrite–quartz veins are surrounded or cut by Pb–Zn-sulfide veins, others occur as independent veins. Six generations of pyrite have been identified at Haopinggou: Py1 to Py3 in Stage 1 and Py4 to Py6 in Stage 2. Pyrites from Stage 1 are enriched in Au, As, Co, Ni, and Bi, whereas Stage 2 pyrites contain higher Ag, Pb, Zn, Sn, and Sb. Invisible Au mostly occurs as lattice-bound gold in Py2 (up to 92 ppm Au) and Py3 (up to 127 ppm Au) and has a close relationship with As. Native Au grains are also present in Py3 and likely resulted from mobilization and reprecipitation of the invisible Au previously locked in the precursor pyrite. This view is supported by extensive plastic deformation in Stage 1 pyrite as revealed by electron backscatter diffraction analysis. In Stage 2, Ag is mostly present as lattice-bound silver closely associated with Sb in galena (up to 798 ppm Ag). A variety of silver minerals are also present as inclusions within galena or as interstitial grains. These silver minerals were likely formed via Ag–Cu exchange reaction between tetrahedrite and galena or represent exsolution from galena due to a temperature decrease. Pb isotopic compositions differ remarkably between Stage 1 and Stage 2 sulfides, indicating different sources of lead. Pb in Stage 2 Pb–Zn-sulfide veins is consistent with the Haopinggou porphyry close to the veins. The field, textural, compositional, and lead isotopic data led us to conclude that the early gold-bearing pyrite–quartz veins and late silver-bearing Pb–Zn-sulfide veins likely formed from distinct fluid systems related to discrete mineralization events. Our study suggests that Au and Ag–Pb–Zn veins hosted in the same metamorphic terrains may not be genetically related to each other.

Introduction

Gold vein deposits in Precambrian metamorphic terrains constitute one of the world's most important gold resources, both in terms of historical production and current reserves (Groves 1993; Groves et al. 1998, 2003; Goldfarb et al. 2005). They typically consist of auriferous quartz–carbonate–sulfide veins and sulfide disseminations and stockworks in hydrothermally altered wall rocks (McCuaig and Kerrich 1998). The sulfide minerals either contain free, visible gold, or refractory, invisible gold (Oberthür et al. 1997; Groves et al. 1998; Goldfarb et al. 2001). Silver–lead–zinc veins also occur widely in many Precambrian metallogenic districts worldwide (Leach et al. 1988; Lynch 1989; Beaudoin and Sangster 1992; Box et al. 2012). They are mostly hosted in greenschist to amphibolite facies metasedimentary terranes (Beaudoin and Sangster 1992, and reference therein) and are commonly controlled by crustal-scale faults and secondary or higher-order structures (Beaudoin et al. 1991; Leach et al. 1998; Li et al. 2013). Although both Au and Ag–Pb–Zn veins occur in metamorphic terrains and commonly have similar geological and alteration features, they are rarely found in the same district (e.g., Leach et al. 1988; Groves et al. 1995). Consequently, whether or not they are genetically related remain poorly understood.

The southern margin of the North China Craton (NCC) is well endowed with Au, Mo, and Ag–Pb–Zn deposits (Mao et al. 2002, 2008), forming one of the most important metallogenic belts in China (Fig. 1). Within this metallogenic belt, the Xiong'ershan district (Fig. 1) contains numerous auriferous quartz-sulfide veins and several Au-bearing breccias (Mao et al. 2002; Chen et al. 2009). Auriferous veins are mostly hosted in Late Archean to Paleoproterozoic high-grade metamorphic rocks or, less significantly, unmetamorphosed late Paleoproterozoic volcanic rocks (Chen and Fu 1992; Mao et al. 2002; Chen et al. 2008; Tang et al. 2013). In the last two decades, a number of Ag–Pb–Zn vein deposits have been discovered in the Xiayu ore field, west of the Xiong'ershan district (Fig. 2; Chen and Guo 1994; Chen et al. 2004; Mao et al. 2006). These veins were localized in the NNE-trending faults cutting the Late Archean high-grade metamorphic rocks. The Shagou, Haopinggou, and Tieluping deposits (Fig. 2) are the best examples of Ag–Pb–Zn veins and are currently the largest Ag producers in the southern NCC.

The Haopinggou deposit in the northern Xiayu ore field (Fig. 2) is the only deposit in the region where both Au and Ag–Pb–Zn veins have been recognized, providing an ideal opportunity to study their formation, evolution, and interrelationships. In this paper, we first present textural and compositional data for pyrite from the Haopinggou deposit to reveal the occurrences, distribution patterns, and enrichment mechanisms of gold and silver. We then use in situ lead isotopic data for galena and pyrite to constrain the metal sources for Au and Ag–Pb–Zn veins. All these data are used to uncover the relationships between gold and Ag–Pb–Zn mineralization at Haopinggou.

Geological setting

The NCC consists of the Western and Eastern Blocks, which are separated by the Trans-North China Orogen formed due to the collision of the two blocks at ca. 1.85 Ga (Zhao et al. 2001). From the late Paleoproterozoic to the end of the Paleozoic, the NCC behaved as a coherent, stable continental block, marked by the relatively continuous deposition of shallow–marine carbonate platform sediments throughout the craton (Yang et al. 1986). Large areas along the margins of the NCC were affected by late Paleozoic to early Mesozoic orogenic events (Chen and Fu 1992; Dong et al. 2011). Collision of the Yangtze and North China Cratons during the Triassic produced the Qinling–Dabie orogenic belt extending for ca. 1500 km (Fig. 1; Li et al. 1993). The subconinental lithospheric mantle

beneath the eastern portion of the NCC has been thinned significantly during the late Jurassic to early Cretaceous (Menzies et al. 1993; Fan et al. 2000; Yang et al. 2008; Zhu et al. 2012). The lithospheric thinning has resulted in voluminous bimodal magmatism (Wu et al. 2005; Mao et al. 2010; Pei et al. 2011), numerous extensional basins (Tian et al. 1992; Ren et al. 2002; Zhu et al. 2010), metamorphic core complexes (Zheng et al. 1991; Zhang and Zheng 1999; Liu et al. 2005), and pervasive hydrothermal mineralization over the entire eastern half of the NCC (Mao et al. 2002, 2008; Li et al. 2006, 2012a, b; Goldfarb and Santosh 2014; Zhu et al. 2015).

The Xiong'ershan district is dominated geologically by the Xiong'ershan metamorphic core complex (MCC), with the Luoning detachment fault separating the lower and upper plates of the complex (Figs. 1, 2; Shi et al. 2004). The lower plate consists of the Late Archean to early Paleoproterozoic metamorphic Taihua Group, including amphibolite, felsic gneiss, migmatite, and metamorphosed supracrustal rocks intercalated with mafic to ultramafic rocks (Hu et al. 1988; Chen and Fu 1992). The upper plate of the MCC consists of the Paleoproterozoic Xiong'er Group and Mesozoic to Cenozoic terrestrial sedimentary rocks (Fig. 1). The Xiong'er Group is composed of volcanic sequences dominated by andesites, with lesser basalts and rhyolites and minor intercalations of clastic rocks (Zhao et al. 2002; Peng et al. 2008). In situ U–Pb isotope data of zircon grains indicate that rocks of the Xiong'er Group were erupted between 1.78 and 1.75 Ga (Zhao et al. 2004; He et al. 2009).

The Xiong'ershan district is bounded structurally by the Luoning Fault to the north and the Machaoying Fault to the south (Fig. 1). The Luoning Fault is a detachment fault of the Xiong'ershan MCC; it is characterized by a well-developed zonation from bottom to top of gently dipping mylonitic rocks, retrograde chloritized breccias, and cataclasites (Shi et al. 2004). The north-dipping Machaoying Fault extends east–west for more than 200 km (Fig. 1). It was generated by the Mesozoic continental collision between the Yangtze and North China Cratons (Hu et al. 1988; Yan et al. 2000; Dong et al. 2011). Geophysical data interpretations have revealed that the Machaoying Fault is a trans-lithospheric structure (Hu et al. 1988). Secondary or higher-order NNE-trending faults are widespread in the district (Fig. 1), notably in the west where major Ag–Pb–Zn veins are developed (Fig. 2). Structural analysis indicates that these faults were characterized by early compressional deformation and then reactivated as late extensional faults (Mao et al. 2006; Gao et al. 2011).

Mesozoic granitoids intruded the Archean and Paleoproterozoic rocks in the Xiong'ershan district and adjacent areas (Fig. 1). The Wuzhangshan and Huashan plutons (Fig. 1) have SHRIMP zircon U–Pb ages of 156.8 ± 1.2 and 132.0 ± 1.6 Ma, respectively (Mao et al. 2010). The Heyu pluton (Fig. 1) is an intrusive complex generated by multiple phases emplaced between 148 and 127 Ma (Guo et al. 2009; Gao et al. 2010; Mao et al. 2010). Many Mo-mineralized granitoid porphyries occur within the Xiong'ershan and Luanchuan districts (Fig. 1). They were emplaced between 158 and 131 Ma as constrained by zircon U–Pb geochronology (Li et al. 2005; Mao et al. 2010).

Geology and mineralization of the Haopinggou Au–Ag–Pb–Zn deposit

The Haopinggou Au–Ag–Pb–Zn deposit is located in the northern portion of the Xiayu ore field (Fig. 2) and is hosted in amphibolite and migmatized felsic to mafic gneiss, with minor marble and magnetite-bearing quartzite of the Taihua Group (Luo et al. 2000). Mesozoic and Cenozoic continental sedimentary rocks are locally present and unconformably overlie the Taihua Group. Northeast-striking extensional faults are common, mostly dipping 60°–85° to the northwest (Fig. 2).

The Haopinggou granite porphyry intruded amphibolites of the Taihua Group to the northwest of the mine (Fig. 2). This porphyry has a SHRIMP zircon U–Pb age of 133.5 ± 1.4 Ma (Ye 2006). A NE-striking breccia body occurs immediately to the southwest of the Haopinggou porphyry. The breccias consist of rocks of the Taihua and Xiong'er Group.

Au–Ag–Pb–Zn mineralization at Haopinggou has been recognized within more than 20 NE-oriented fault zones (Figs. 2, 3), but only several of them contain industrial ore bodies. The H15, H16, and H17 veins are the most important, accounting for ca. 75 % of the proven reserves of the deposit. To 2013, the deposit has proven and probable reserves of 43.8 Koz Au at an average grade of 1.18 g/t, and 4.0 Moz Ag at an average grade of 107 g/t, 54.6 Kt Pb at 4.71 wt%, and 14.3 Kt Zn at 1.24 wt% (Stephenson et al. 2014). Potential for new discoveries has been highlighted by a recent deep drill hole that uncovered a 1.42-m-wide ore shoot at −82 m, with average grades of 263 g/t Au, 335 g/t Ag, 0.73 wt% Pb, and 1.74 wt% Zn (Silvercorp Metals INC., unpub. data).

A majority of mineralized veins at Haopinggou strike northeast and dip 50°–85° NW. They are 600–2100 m long and continue for several hundred meters down plunge. Individual veins contain more than one ore body, with high-grade shoots separated by subeconomic or unmineralized segments. The ore bodies typically consist of an early pyrite–quartz assemblage (Stage 1) and a late Pb–Zn-sulfide assemblage (Stage 2). There are clear crosscutting relationships between the two stages (e.g., Fig. 3a, b), with the Stage 2 Pb–Zn-sulfide veins containing fragments of Stage 1 pyrite–quartz veins (Fig. 3c). Metallic minerals in Stage 1 pyrite–quartz veins are dominated by pyrite, with minor to trace amounts of chalcopyrite, pyrrhotite, arsenopyrite, galena, sphalerite, native gold, electrum, and kustelite (Fig. 3a–e). The gangue minerals are mainly quartz and siderite (Fig. 3a, b, d, e). Stage 2 Pb–Zn-sulfide veins are dominated by sphalerite, galena, and pyrite, with subordinate chalcopyrite, tetrahedrite, and a variety of silver minerals (Fig. 3a–c, e, f), associated with quartz, ankerite, and calcite (Fig. 3a–b, f).

The mineralized veins are surrounded by alteration halos ranging from 10 cm to 2 m in width (Fig. 3a–c). The alteration assemblages consist mainly of sericite, quartz, chlorite, and carbonate, with minor disseminations of sulfide minerals (e.g., pyrite, chalcopyrite, and galena). The Haopinggou breccia body, located west of the mine (Fig. 2), mainly consists of rocks of the Taihua Group and the Xiong'er Group. The breccia body is barren in gold mineralization, although pyrite, sphalerite, galena, quartz, and carbonate occur as hydrothermal cements in areas where it is intersected by NE-striking faults.

Samples and analytical methods

Samples used for this study were collected from underground work areas, mainly from the economically most important H15, H16, and H17 veins. Sample details are summarized in Table 1. Polished thick and thin sections from each sample were examined petrographically in order to characterize mineralogy, textures, and paragenesis. Acid etching (HNO_3) was used to reveal internal textures in pyrite grains. Selected thin sections were analyzed by a JEOL Quanta-200 environmental scanning electron microscope (SEM) equipped with an energy dispersive spectrometer (EDS), which enabled combined analysis of morphology and major element compositions of phases of interest. Electron microprobe (EMP) analyses of the ore minerals were performed using a JXA-8100 superprobe. Standards and unknowns were analyzed using a 5-μm beam diameter, an accelerating voltage of 20 kV, and a beam current of 20 nA. The standards, spectral lines, and detection limits (ppm) for each element are: Fe (FeS_2, Kα, 110), Cu (Cu, Kα, 120), Zn (ZnS, Kα, 160), S (FeS_2, Kα, 50),

As (GaAs, Lα, 200), Sb (Sb, Lα,110), Cd (Cd, Lα, 260), Te (Te, Lα, 150), Co (Co, Kα, 100), Ni (Ni, Kα, 80), Ag (Ag, Lα, 70), and Au (Au, Lα, 250). The data were reduced using the ZAF correction method. Crystallographic orientation data of pyrite were collected by indexing EBSD Kikuchi patterns using an Oxford Instruments HKL Nordlys II EBSD detector coupled to a FEI Quanta 450 field emission gun SEM. The analyses were operated at 15 kV, 25 mm working distance and 70° sample tilt in high vacuum mode. Orientation maps of pyrite were acquired in automatic mode with a step size of 1 or 5 μm. All the above experiment equipments are hosted at the State Key Laboratory of Geological Processes and Mineral Resources (GPMR), China University of Geosciences, Wuhan.

In situ trace element analyses of pyrite

In situ trace element analyses of pyrite were conducted using laser ablation-inductively coupled plasma mass spectroscopy (LA-ICPMS) at the Center of Excellence in Ore Deposits (CODES), University of Tasmania, Australia. Analytical instrumentation consists of a New Wave 213-nm solid-state laser microprobe and an Agilent 7500a Quadrupole ICP-MS. The operating conditions and procedures applied to pyrite have been detailed in Large et al. (2007, 2009) and Danyushevsky et al. (2011).

Spot analyses of pyrite were performed by laser-ablating spots of 35 μm diameter. The repetition rate was 5 Hz, and laser beam energy was maintained between 4 and 5 J/cm^2. Analysis time was 90 s, consisting of 30-s background (laser off) and 60-s analysis (laser on). Calibration was performed using an in-house reference material STDGL2b2 (Danyushevsky et al. 2011), which was analyzed twice every 1.5 h to correct for instrument drift (100-μm beam size at 5 Hz). Data reduction was made using SILLS software following standard methods (Longerich et al. 1996). Iron was used as the internal standard, and the Fe contents were quantified by EMP analyses. Imaging of trace element distributions in pyrite was performed by ablating a set of parallel lines arranged in a grid over the sample. Beam diameters were 12, 15, or 22 μm depending on sample size. The beam was rastered at 10-Hz repetition rate and at a speed equal to the beam size per second. Redeposition of sample back onto the surface was controlled by preablating each line prior to analysis. Images were produced for each element using a logarithmic color scale.

In situ Pb–Pb isotope analyses of galena

In situ Pb–Pb isotope analyses of galena were performed using a Nu Plasma HR multi-collector ICPMS coupled to a Photon Machine Analyte G2 laser ablation system at the Geological Survey of Finland in Espoo, Finland. The MC-ICP-MS is equipped with nine Faraday detectors and amplifiers with 10^{11} Ω resistors. Baseline and ablation data were measured on peak, collected in static mode (^{208}Pb, ^{207}Pb, ^{206}Pb, ^{204}Pb, ^{205}Tl, ^{203}Tl). The raw data were filtered at 2 s and corrected for mass discrimination using an exponential law. The mass discrimination factor for Pb was determined using a ~20 ppb Tl solution nebulized at the same time as the sample, using a desolvating nebulizer. Samples were ablated in He gas (gas flows = 0.4 and 0.1 l/min) within a HelEx ablation cell (Müller et al. 2009). The gas mixture was optimized daily for maximum sensitivity. All analyses were made using rasters with a stage stepping speed of 1 micron/second. Ablation conditions were: 5 μm beam diameter; 5 Hz pulse frequency; 1.4 J/cm^2 beam energy density. A single Pb–Pb measurement included 1-min baseline measurement (measure zero) prior to a batch of ratio measurements, each of the latter consisting of data acquisition for 45 s with laser on. Breaks in an analytical session, or refilling the Tl solution necessitated a new measure zero.

A galena from Broken Hill was used to monitor the precision and accuracy of the measurements. It was analyzed every ten samples over the entire period of analysis. The obtained accuracy is estimated to be equal to or better than 3 ‰ for $^{208}Pb/^{204}Pb$, 2 ‰ for $^{207}Pb/^{204}Pb$, 2 ‰ for $^{206}Pb/^{204}Pb$, and 0.34 ‰ for $^{207}Pb/^{206}Pb$ (2σ), compared with the certified value of Townsend et al. (1998) and Stevenson and Martin (1986).

In situ Pb–Pb isotope analyses of pyrite

In situ lead isotope analyses of pyrite were performed on a Neptune Plus MC-ICP-MS (Thermo Fisher Scientific, Dreieich, Germany) equipped with a Geolas 2005 excimer ArF laser ablation system (Lambda Physik, Göttingen, Germany) at the State Key Laboratory of Geological Processes and Mineral Resources, China University of Geosciences, Wuhan. In the laser ablation system, helium was used as the carrier gas for the ablation cell and was mixed with argon (makeup gas) after the ablation cell. The spot diameter ranged from 44 to 90 μm dependent on Pb signal intensity. The pulse frequency was from 4 to 10 Hz, but the laser fluence was kept constant at ~3 J/cm^2. A new signal-smoothing and mercury-removing device was used downstream from the sample cell to efficiently eliminate the short-term variation of the signal and remove the mercury from the background and sample aerosol particles (Hu et al. 2014). The Neptune Plus was equipped with nine Faraday cups fitted with 10^{11} Ω resistors. Isotopes ^{208}Pb, ^{207}Pb, ^{206}Pb, ^{204}Pb, ^{205}Tl, ^{203}Tl, and ^{202}Hg were collected in Faraday cups using static mode. The mass discrimination factor for Pb was determined using a Tl solution (NIST SRM 997) nebulized at the same time as the sample, using an Aridus II desolvating nebulizer. The ^{202}Hg signal was used to correct the remaining ^{204}Hg interference on ^{204}Pb, using the natural $^{202}Hg/^{204}Hg$ ratio.

In this method, the natural Tl isotopic composition was assumed. MASS-1, a sulfide standard reference from USGS (Wilson et al. 2002), and two in-house standards PY-3 and Sph-2 were then run to define the mathematical relationship between Tl and Pb mass bias (Woodhead 2002). The Pb isotopic compositions of those three sulfides samples were previously determined by solution-MC-ICP-MS at GPMR. MASS-1 was used to monitor the precision and accuracy of the measurements after ten sample analyses, over the entire period of analysis. The obtained accuracy is estimated to be equal to or better than ±0.6 ‰ for $^{208}Pb/^{204}Pb$, $^{207}Pb/^{204}Pb$, and $^{206}Pb/^{204}Pb$ compared to the solution value by MC-ICP-MS, with a typical precision of 0.4 ‰ (2σ).

Results

Gold and silver mineralogy

Stage 1 pyrite–quartz veins contain abundant visible gold minerals, including native gold, electrum, and kustelite (Fig. 4; Table 2). They occur as anhedral to subhedral inclusions within pyrite and, less commonly, in magnetite, siderite, and quartz. They are also locally present as small grains along grain boundaries of the host minerals. Native gold is mostly hosted in siderite and magnetite (Fig. 4a, b). It contains 85.9–93.9 wt% Au and 5.3–12.5 wt% Ag, with a mean gold fineness of 905 (Table 2). Electrum is the most abundant gold mineral, commonly enclosed in or marginal to pyrite, magnetite, or siderite (Fig. 4b–e). The Au and Ag contents in electrum are 69.8–75.0 wt% and 23.5–27.9 wt%, respectively (Table 2). Kustelite typically occurs as inclusions in siderite (Fig. 4e, f), and it has

comparable Au (46.3–53.8 wt%) and Ag (44.5–52.6 wt%) contents (Table 2). Traces of Cu, Zn, and Fe are also detected in the gold-bearing minerals (Table 2).

Silver-bearing minerals are widespread and abundant in Stage 2 Pb–Zn-sulfide veins, mainly including tetrahedrite, argentiferous tetrahedrite, stromeyerite, pyrargyrite, polybasite, argentite, and native silver (Fig. 5; Table 2). They occur as microscopic aggregates within galena, sphalerite, and chalcopyrite, as interstitial grains between the major minerals, or as stringers infilling Pb–Zn-sulfide grains (Fig. 5). Tetrahedrite has a close paragenetic relationship with chalcopyrite and is locally equilibrated with polybasite (Fig. 5a) or argentiferous tetrahedrite. Tetrahedrite contains 1.56–6.69 wt% Ag, 0.28–1.44 wt% Fe, 34.48–37.40 wt% Cu, and 6.31–7.08 wt% Zn (Table 2). Argentiferous tetrahedrite, the most common silver mineral at Stage 2, occurs as veinlets within sphalerite (Fig. 5b) and as inclusions or aggregates in galena (Fig. 5c) and chalcopyrite (Fig. 5f). Compared to tetrahedrite, argentiferous tetrahedrite contains higher Ag (18.39–28.09 wt%) and Fe (2.04–2.80 wt%) coupled with lower Cu (17.83–24.34 wt%) and Zn (4.11–4.98 wt%; Table 2). The contents of Sb (22.90–25.61 wt%) and As (1.02–2.68 wt%) are relatively homogeneous both in tetrahedrite and argentiferous tetrahedrite (Table 2). Stromeyerite, commonly coexisting with argentiferous tetrahedrite and chalcopyrite, occurs as fracture fillings in sphalerite (Fig. 5b). Stromeyerite has highly variable Ag and Cu contents ranging from 28.70 to 61.62 and 16.56 to 42.05 wt%, respectively (Table 2). Polybasite also has a widespread distribution and is intergrown with other silver minerals such as pyrargyrite (Fig. 5c, d). The contents of Ag and Sb are 59.75–60.56 and 21.29–22.63 wt% in pyrargyrite and 71.32–77.06 and 4.96–9.95 wt% in polybasite (Table 2). Argentite occurs in textural equilibration with polybasite and native silver (Fig. 5e, f) and contains 79.49–84.34 wt% Ag (Table 2). Native silver consists of 97–98 wt% Ag with minor Au (0.27–0.40 wt%) and Cu (0.45–1.11 wt%; Table 2). Gold contents are generally very low (<0.4 wt%; Table 2) in all silver minerals. Textural relationships indicate a paragenetic sequence for the silver minerals consisting of, in an order of precipitation, tetrahedrite, argentiferous tetrahedrite and stromeyerite, pyrargyrite and polybasite, and agentite and native silver (Fig. 5). This implies that the late-stage minerals became progressively more enriched in Ag (Table 2).

Pyrite textures

Pyrite is the predominant sulfide mineral both in Stage 1 and 2 veins. Petrographic observations of acid-etched thin sections and back-scattered electron imaging revealed six generations of pyrite (Fig. 6), with three (Py1-3) from Stage 1 pyrite–quartz veins and the other three (Py4-6) from Stage 2 Pb–Zn-sulfide veins. The first generation (Py1) is coarse-grained pyrite with abundant fine-grained inclusions of quartz, chalcopyrite, and galena (Fig. 6a, b). The second generation (Py2) consists of masses of subhedral to euhedral pyrite overgrowths on Py1 (Fig. 6a, b). Py2 is texturally homogeneous and rarely contains mineral inclusions. Py3 typically occurs as overgrowths of Py1 and Py2 and is also present as discrete subhedral to euhedral grains (Fig. 6a, c). Py3 contains abundant galena and chalcopyrite inclusions, but differs from Py1 in that it hosts numerous native gold and electrum grains (Fig. 6c).

In Stage 2 Pb–Zn-sulfide veins, Py4 generally has porous textures and contains abundant inclusions of chalcopyrite, ankerite, and lesser quartz (Fig. 6d, e). Py5 encloses Py4 and is characterized by subhedral to euhedral and texturally homogeneous clean grains (Fig. 6d–f). Py6 has overgrown Py5 and is characterized by the presence of numerous galena, sphalerite, and quartz inclusions (Fig. 6f).

Field and petrographic observations suggest plastic deformation of pyrite from Stage 1 veins (Fig. 3b, d). The deformation is confirmed and further characterized by results of EBSD analysis (Fig. 7). The orientation contrast image (OCI) and colored EBSD image (Fig. 7b, c) of pyrite from sample HP32 provide additional evidence for the plastic deformation of the studied pyrite grains. In addition, the scattered pole figures of pyrites show an anticlockwise rotation in the range of 0°–15° around one [100] axis of pyrite (Fig. 7d), indicating that the apparent grains or subgrains are inherited from a single former parent pyrite grain. Euler orientation image and matched scattered pole figures of another pyrite aggregate from sample HP41 (Fig. 7e) confirm that this aggregate consists of several pyrite grains with different crystallographic orientations (Fig. 7f, h). The colored EBSD map shows a range of 0°–4° for the crystallographic misorientations of one selected grain (Fig. 7g), which is interpreted as reflective of low-angle subgrain boundaries resulted from intragranular plastic deformation.

Trace element compositions of pyrite

A total of 91 LA-ICPMS spot analyses were completed on various generations of pyrite from Haopinggou. A total of 26 elements were analyzed: Cr, Mn, Fe, Co, Ni, Cu, Zn, Ga, As, Se, Mo, Ag, Cd, Sn, Sb, Te, Ba, Gd, Hf, Ta, W, Pt, Au, Tl, Pb, and Bi. The results are given in ESM 1. Selected trace element compositions of Py1 to Py6 are illustrated in Fig. 8. Representative time-resolved LA-ICPMS spectra for each generation of pyrite recorded during spot analyses are shown in Fig. 9. In addition to spot analyses, LA-ICPMS element mapping was conducted on six grains to characterize the distribution patterns of trace element in the various pyrite generations, involving Au, As, Ag, Mn, Co, Ni, Cu, Zn, Pb, Bi, Te, Se, Sn, Ti, Cd, Mo, W, S, Fe, Zr, Al, Si, V, K, and Ca. Three representative sets of LA-ICPMS element images are shown in Figs. 10 and 11.

Py1 contains higher Co (mean 179 ppm) and Ni (453 ppm) compared to Py2. Other elevated trace elements in Py1 include Ag (mean 5.6 ppm), Pb (74 ppm), Cu (269 ppm), Sb (4.6 ppm), and Bi (4.3 ppm). Notably, Py1 has low Au (<0.02–0.47 ppm) and highly variable As (3–1741 ppm). In sharp contrast, Py2 has much higher contents of As (mean 2363 ppm) and Au (9.3 ppm) but other trace elements are generally very low compared to Py 1 (e.g., <71 ppm Cu, <6 ppm Zn, and 0.02–111 ppm Pb). Py3 is enriched in As (mean 1534 ppm), Au (19.1 ppm), Ag (25.9 ppm), Pb (1853 ppm), Bi (19.6 ppm), Sb (5.2 ppm), Cu (210 ppm), Co (820 ppm), and Ni (336 ppm). Results of the spot analyses for Py1, Py2, and Py3 are consistent with and confirmed by the LA-ICPMS time-resolved spectra that show the ion signal intensities of the trace elements (Fig. 9a–c). LA-ICPMS images of pyrite from Stage 1 pyrite–quartz veins also reveal spectacular compositional zoning patterns (Fig. 10), which correspond to distinct generations of pyrite revealed by petrographic observation of acid-etched grains. Figure 10a highlights three generations of a selected pyrite grain: the porous and inclusion-rich core (Py1) has elevated Ag, Pb, Cu, Sb, Bi, Zn, Cd, and Sn, whereas the overgrowth (Py2) has relatively high concentrations of As and Au compared to Py 1. The thin rim (Py3) has high concentrations of Co, Ni, As, Au, Ag, Pb, Cu, and Bi. Similar distribution patterns of trace elements in Py1 and Py2 are also observed in another pyrite grain (Fig. 10b). The microfractures within this grain are enriched in gold and other trace elements (e.g., As, Ag, Pb, Bi, and Cu), with two gold nanoparticles being observed (Fig. 10b).

Py4 has elevated concentrations of Ag (mean 62 ppm), Sb (7.9 ppm), Cu (317 ppm), Pb (109 ppm), Zn (910 ppm), Co (158 ppm), and Ni (333 ppm), but Au is extremely low (<0.01–0.25 ppm) and As ranges from below detection limit to 830 ppm. Compared to Py4, Py5 is enriched in As (mean 1224 ppm), but depleted in most other trace elements (e.g., <1.2 ppm Ag, <4 ppm Cu, <37 ppm Pb, and

<0.5 ppm Zn), with low Au contents (<0.01–0.51 ppm). Py6 contains unusually high concentrates of Pb (mean 6120 ppm) that most likely result from abundant microinclusions of galena (Fig. 6f). Other trace elements include Ag (mean 43 ppm), Au (0.69 ppm), Cu (118 ppm), Zn (22.7 ppm), and Sb (10.2 ppm), all much higher than values of Py5. The spot analysis results for Py4 to Py6 are consistent with their LA-ICPMS spectra (Fig. 9d–f). LA-ICPMS element images of pyrite grains from the Pb–Zn-sulfide veins also show conspicuous compositional zoning (Fig. 11). Figure 11 shows a porous core (Py4) enriched in Ag, Pb, Cu, Zn, Sb, Mn, Co, and Ni, and a rim (Py5) that has elevated As and Au compared with Py4.

Lead isotope compositions of galena and pyrite

In situ lead isotope data of galena are listed in ESM 2. Thirty-nine galena grains analyzed from Stage 1 pyrite–quartz veins have $^{206}Pb/^{204}Pb$ ratios of 17.624–17.811, $^{207}Pb/^{204}Pb$ of 15.473–15.503, and $^{208}Pb/^{204}Pb$ of 38.245–38.319. Nine galena grains from Stage 2 Pb–Zn-sulfide veins have $^{206}Pb/^{204}Pb$ ratios of 18.128–18.173, $^{207}Pb/^{204}Pb$ of 15.527–15.544, and $^{208}Pb/^{204}Pb$ of 38.471–38. 508.

In situ lead isotope data of pyrite are listed in ESM 3. There are no obvious isotopic variations among different generations of pyrite from each individual stage. Lead isotopic compositions of five pyrite grains from Stage 1 range between 17.640 and 17.671 for $^{206}Pb/^{204}Pb$, 15.487 and 15.508 for $^{207}Pb/^{204}Pb$, and 38.270 and 38.345 for $^{208}Pb/^{204}Pb$. Twenty pyrite grains from Stage 2 have $^{206}Pb/^{204}Pb$ ratios of 18.130–18.290, $^{207}Pb/^{204}Pb$ of 15.502–15.565, and $^{208}Pb/^{204}Pb$ of 38.481–38.572.

Discussion

Occurrence and enrichment mechanism of gold

Numerous studies have shown that gold in sulfide minerals either occurs as visible grains or as invisible nanoparticles and lattice-bound solid solutions (Cabri et al. 1989; Cook and Chryssoulis 1990; Reich et al. 2005; Fougerouse et al. 2016a). Precipitation of gold is affected by several factors, including concentration and chemical state of gold in the ore fluids, temperature, pH, oxygen and sulfur fugacity, and metamorphic history (Heinrich and Eadington 1986; Cathelineau et al. 1989; Cabri et al. 2000; Reich et al. 2005; Large et al. 2007; Morey et al. 2008). Recent research highlights the importance of sulfide growth rate on controlling the distribution of nanoscale gold clusters in auriferous sulfides (Fougerouse et al. 2016c). Pyrite and arsenopyrite are among most important Au-bearing minerals, and Au-bearing pyrite is commonly high in arsenic, which is believed to be favorable for co-precipitation of Au in the pyrite structure (e.g., Cook and Chryssoulis 1990; Pals et al. 2003; Reich et al. 2005; Sung et al. 2009).

At Haopinggou, Au is significantly enriched in Stage 1 pyrite–quartz veins ($P < 0.05$ by statistical t test), whereas Stage 2 Pb–Zn-sulfide veins are basically devoid of gold (Fig. 12a). In Stage 1, porous Py1 grains have low Au contents (below or marginally above the detection limit; ESM 1) and minor amounts of Ag (mean 5.6 ppm). Py2 is characterized by elevated Au (mean 9.3 ppm) and As (mean 2363 ppm) and yields relatively smooth LA-ICPMS spectra for Au and As (Fig. 9b), indicating a predominance of lattice-bound gold in the As-rich pyrite, consistent with element maps (Fig. 10). Py3 is enriched both in Au (mean 19.14 ppm) and Ag (mean 25.94 ppm), which are most likely present as microinclusions of Au–Ag compounds in view of the coincident spiky signals of Au and Ag in the LA-ICPMS spectra (e.g., Fig. 9c). This view is consistent with petrographic observations of abundant inclusions of electrum and base-metal sulfides in Py3 (e.g., galena, chalcopyrite; Figs. 4c, d, 6c).

In summary, invisible Au is present mostly in Py2 and Py3 (Figs. 8a, b, 9b, c), whereas Au inclusions have been observed in Py3, siderite, and magnetite (Figs. 4, 6c). Based on results of LA-ICPMS spot analyses and trace element imaging, there is a positive correlation between Au and As in Stage 1 pyrite (Figs. 9, 12b). Similar positive correlations of these elements have been reported from orogenic-type and carlin-type gold deposits worldwide (e.g., the Sukhoi Log deposit in Siberia, the northern Carlin Trend in Nevada), where they have been interpreted to reflect a predominance of invisible gold in arsenian pyrite (e.g., Cook and Chryssoulis 1990; Ashley et al. 2000; Pals et al. 2003; Reich et al. 2005; Sung et al. 2009; Large et al. 2009). Most LA-ICPMS spot analyses of arsenian Py2 and Py3 plot below the gold saturation line in Fig. 12b, confirming that gold in Py2 and Py3 occurs mostly likely as invisible gold.

Previous studies have shown that invisible Au and associated trace elements locked in the lattice of sulfide minerals can be liberated during subsequent deformation, metamorphism, and/or hydrothermal overprints, leading to reprecipitation of visible gold particles on grain boundaries or microfractures (Mumin et al. 1994; Vaughan and Kyin 2004; Morey et al. 2008; Sung et al. 2009; Cook et al. 2009; 2013; Reddy and Hough 2013; Fougerouse et al. 2016b). Three mechanisms may explain the mobilization of trace element at mineral scale: (1) fluid-mediated replacement (Putnis 2009; Sung et al. 2009; Harlov et al. 2011; Fougerouse et al. 2016a, b); (2) intragrain diffusion (Reddy et al. 2006, 2007; Reddy and Hough 2013; Vukmanovic et al. 2014); and (3) partial melting of the sulfide ore (Mavrogenes 2001; Tomkins et al. 2004; Ciobanu et al. 2006). At Haopinggou, Stage 1 pyrite grains are marked by plastic deformation (Figs. 3b, d, 7), which could have generated lattice dislocations and orientation boundaries (Fig. 7) that in turn facilitated intragrain diffusion through fast pathways (e.g., Reddy and Hough 2013) and fluid-mediated liberation (e.g., Fougerouse et al. 2016b) of invisible Au. The remobilized Au can be efficiently scavenged by deformation-related fluids and reprecipitated as particles within microfractures of the same pyrite grain or included in overgrowths surrounding the parental grains (Figs. 6c, 7, 10) and nearby gangue minerals (Fig. 4a–d). A similar process has been documented at El Callao gold district, Venezuela (Velásquez et al. 2014). Py3 at Haopinggou is enriched in many other trace elements, especially chalcophile elements including Cu, Pb, Bi, Sb, Te, and Ag (Fig. 8a, b). In addition, chalcopyrite and galena are intergrown with gold minerals as inclusions in Py3 or within microfractures (Figs. 6c, 10b). Thus, those chalcophile elements could also have been remobilized from earlier pyrite together with Au during the deformation process.

Occurrence and enrichment mechanism of silver

Silver is enriched in pyrite from Stage 2 Pb–Zn-sulfide veins at Haopinggou, particularly in Py4 (mean 64 ppm) and Py6 (mean 43 ppm). Laser ablation ICP-MS time-resolved spectra and element images of Py4 show that Ag is positively correlated with Pb, Cu, Zn, and Sb (Figs. 9d, 11), indicating that the elevated Ag is related to microinclusions of base-metal sulfides, particularly galena. A similar scenario is noted in Py6, which contains numerous inclusions or stringers of galena and sphalerite (Fig. 6f). Representative LA-ICPMS spectra for Py6 show extremely high Pb (up to 1.4 wt%), providing additional evidence for the presence of galena microinclusions in pyrite (Fig. 9f). The spectrum of Ag is parallel to that of Pb and Sb, confirming that Ag occurs mainly in inclusions of galena or Sb-bearing silver minerals (Fig. 9f).

A close association of Ag and galena has been documented in many ore deposits (e.g., Sharp and Buseck 1993; Lueth et al. 2000; Zeng et al. 2000; Costagliola et al. 2003). Silver can enter into the crystal lattice of galena together with Sb (or Bi) by substitution for Pb as illustrated in the formula $Ag^{+} + (Sb, Bi)^{3+} = 2Pb^{2+}$. The maximum solubility of Ag in galena can be up to 9.4 wt% at 350–400 °C (Foord et al. 1988; Foord and Shawe 1989). Both Py4 and Py6 from Stage 2 Pb–Zn-sulfide veins contain abundant galena inclusions (Fig. 6d–f) and yield flat LA-ICPMS spectra indicating elevated but uniform Ag and Sb (Fig. 9d, f), further demonstrating that Ag enrichment in pyrite grains is largely caused by the galena inclusions. This interpretation is also confirmed by the LA-ICPMS element images (Fig. 11) and positive correlations between Pb and Ag (Fig. 12c), and Ag and Sb (Fig. 12d).

Silver can be incorporated into tetrahedrite to form argentiferous tetrahedrite (Fig. 13a) via an Ag–Cu solid-state exchange reaction (Sack et al. 2002, 2003). Silver can also form minerals via exsolution of silver from galena (Fig. 13b) due to decreasing temperatures (Sharp and Buseck 1993; Chutas et al. 2008; Voudouris et al. 2011). These silver minerals include, in order of precipitation, argentiferous tetrahedrite and stromeyerite, pyrargyrite and polybasite, and argentite and native silver (Fig. 5). At Haopinggou, Ag is progressively enriched whereas Cu becomes progressively depleted in paragenetically late silver minerals (Table 2). According to the fractional crystallization model of Hackbarth and Petersen (1984), progressive Ag enrichment in paragenetically late minerals can be explained in terms of preferential removal of Cu from the ore-forming solution by precipitation of Cu-bearing minerals (chalcopyrite, tetrahedrite, etc.)

Two mineralizing events at Haopinggou

Field relations at Haopinggou indicate that the gold-mineralized pyrite–quartz veins predated the silver-mineralized Pb–Zn-sulfide veins (Fig. 3a–c). These two stages either formed from a single, evolving hydrothermal system, or from two spatially overlapping but temporally distinct hydrothermal systems that were associated with different metallogenic events. The following observations and considerations led us to conclude that Stage 1 pyrite–quartz veins and Stage 2 Pb–Zn-sulfide veins are the results of two discrete mineralizing events:

1. The two vein assemblages formed under different structural regimes. Stage 1 pyrite–quartz veins display well-developed foliations (Fig. 3a, b, d), indicating that they have undergone post-mineralization plastic deformation. Results of the EBSD analysis confirm grain-scale plastic deformation for pyrite grains of Stage 1 veins (Fig. 7). In contrast, Stage 2 Pb–Zn-sulfide veins are characterized by open-space filling textures (Fig. 3b, c) and lack deformation, consistent with formation under an extensional tectonic regime with no post-mineralization deformation;

2. The trace element patterns in pyrite from Stage 1 pyrite–quartz and Stage 2 Pb–Zn-sulfide veins are remarkably different. Stage 1 pyrite is enriched in Au, As, Bi, Co, and Ni, whereas Stage 2 pyrite contains much higher Ag, Pb, Zn, and Sb (Fig. 8e);

3. The lead isotopic compositions of sulfide from Stage 1 pyrite–quartz and Stage 2 Pb–Zn-sulfide veins are distinctly different. In the $^{207}Pb/^{204}Pb$ versus $^{206}Pb/^{204}Pb$ diagram (Fig. 14), most of the Stage

2 ores have lead isotopic compositions consistent with that of the Cretaceous Haopinggou porphyry, suggesting that the Pb–Zn-sulfide veins have a magmatic source for Pb and, by inference, Zn and Ag. One Pb–Zn-sulfide vein sample has sericite $^{40}Ar/^{39}Ar$ age of 134.9 ± 0.8 Ma that agree with a zircon U–Pb age of 133.5 ± 1.1 Ma for the Haopinggou porphyry (Ye 2006). The age consistency confirms a magmatic source for the stage 2 veins. In comparison, Stage 1 sulfides have lower $^{206}Pb/^{204}Pb$, $^{207}Pb/^{204}Pb$, and $^{208}Pb/^{204}Pb$ ratios (ESMs 2, 3; Fig. 14), which are distinctly different from values of the Haopinggou porphyry (Fig. 14) and thus rule out a genetic relation between the two.

Taken together, the field, textural, compositional, and isotopic data indicate that Stage 1 and Stage 2 veins at Haopinggou formed under contrasting tectonic regimes and are related to different mineralization events (Fig. 15). Stage 2 Pb–Zn-sulfide veins are likely related to magmatism presumably represented by the Haopinggou porphyry, but genesis of the Stage 1 quartz-pyrite veins remains uncertain. To the east of the Xiayu ore field, numerous Triassic gold veins have been recognized, as best illustrated by the Shanggong and Dianfang gold deposits (Fig. 1), which have been considered to be the result of the orogenic deformation due to collision of the Yangtze and North China Cratons (Chen et al. 2008; Tang 2014). Considering that Stage 1 gold mineralization predates Stage 2 Ag–Pb–Zn mineralization, we tentatively infer that gold mineralization at Haopinggou could have formed in the Triassic. Further geochronological and geochemical investigations are needed to better understand the evolution of the Haopinggou deposit, particularly the age and genesis of the stage 1 auriferous quartz-sulfide veins.

Conclusions

The Haopinggou deposit consists of two distinct mineralization stages with distinct mineral assemblages and trace element compositions. Stage 1 pyrite–quartz veins are dominated by gold mineralization with negligible Ag, whereas the Stage 2 Pb–Zn-sulfide veins are characterized by silver mineralization without Au enrichment. Different generations of pyrite (Py1 to Py3 of Stage 1; Py4 to Py6 of Stage 2) record compositional evolution of the deposit. Stage 1 pyrites are enriched in Au, As, Co, Ni, and Bi, whereas Stage 2 pyrites contain much higher Ag, Pb, Zn, Sn, and Sb. Both visible and invisible gold are present in Stage 1 pyrite–quartz assemblages. The invisible Au is mostly lattice-bound in arsenian Py2, whereas visible Au occurs as inclusions in Py3 and associated metallic and gangue minerals. Similarly, both invisible and visible Ag are present in Stage 2 Pb–Zn-sulfide veins. Invisible Ag is mostly hosted in the lattices of galena and has a positive correlation with Sb, whereas visible Ag is represented by a variety of silver minerals included in galena or interstitial to sulfide or gangue minerals. Lead isotopes of sulfide minerals, combined with textural, geochronological and geological data, allow that the Stage 2 Pb–Zn-sulfide veins are genetically related to early Cretaceous magmatism presumably represented by the Haopinggou porphyry proximal to the veins, whereas the Stage 1 pyrite–quartz veins may have formed during the Triassic orogeny due to collision of the Yangtze and North China Cratons. This study highlights that Au and Ag–Pb–Zn veins may occur in the same metamorphic terrains and share similar geological and alteration features, but may have no genetic relation to each other.

References

Ashley PM, Creagh CJ, Ryan CG (2000) Invisible gold in ore and mineral concentrates from the Hillgrove gold-antimony deposits, NSW, Australia. Miner Depos 35:285–301

Beaudoin G, Sangster DF (1992) A descriptive model for silver–lead–zinc veins in clastic metasedimentary terranes. Econ Geol 87:1005–1021

Beaudoin G, Taylor BE, Sangster DF (1991) Silver–lead–zinc veins, metamorphic core complexes, and hydrologic regimes during crustal extension. Geology 19:1217–1220

Box SE, Bookstrom AA, Anderson RG (2012) Origins of mineral deposits, Belt-Purcell Basin, United States and Canada: an introduction. Econ Geol 107:1081–1088

Cabri LJ, Chryssoulis SL, de Villiers JP, Laflamme JG, Buseck PR (1989) The nature of “invisible” gold in arsenopyrite. Can Mineral 27:353–362

Cabri LJ, Newville M, Gordon RA, Crozier ED, Sutton SR, Mcmahon G, Jiang DT (2000) Chemical speciation of gold in arsenopyrite. Can Mineral 38:1265–1281

Cathelineau M, Boiron MC, Holliger P, Marion P, Denis M (1989) Gold in arsenopyrites: crystal chemistry, location and state, physical and chemical conditions of deposition. Econ Geol Monogr 6:328–341

Chen YJ, Fu SG (1992) Gold mineralization in West Henan. China Seismological Press, Beijing, 234 pp (in Chinese with English abstract)

Chen W, Guo SR (1994) The geological characteristics of the Haopinggou Ag–Pb–Au deposit in Luoning, Henan. Geol Explor Nonferr Metals 3:336–341 (in Chinese with English abstract)

Chen YJ, Pirajno F, Sui YH (2004) Isotope geochemistry of the Tieluping silver-lead deposit, Henan, China: a case study of orogenic silver-dominated deposits and related tectonic setting. Miner Depos 39:560–575

Chen YJ, Pirajno F, Qi JP (2008) The Shanggong gold deposit, Eastern Qinling Orogen, China: isotope geochemistry and implications for ore genesis. J Asian Earth Sci 33:252–266

Chen YJ, Pirajno F, Li N, Guo DS, Lai Y (2009) Isotope systematics and fluid inclusion studies of the Qiyugou breccia pipe-hosted gold deposit, Qinling Orogen, Henan province, China: implications for ore genesis. Ore Geol Rev 35:245–261

Chutas NI, Kress VC, Ghiorso MS, Sack RO (2008) A solution model for high-temperature PbS–AgSbS2–AgBiS2 galena. Am Mineral 93:1630–1640

Ciobanu CL, Cook NJ, Damian F, Damian G (2006) Gold scavenged by bismuth melts: an example from Alpine shear-remobilizates in the Highiş Massif, Romania. Mineral Petrol 87:351–384

Cook NJ, Chryssoulis SL (1990) Concentrations of invisible gold in the common sulfides. Can Mineral 28:1–16

Cook NJ, Ciobanu CL, Mao J (2009) Textural control on gold distribution in As-free pyrite from the Dongping, Huangtuliang and Hougou gold deposits, North China Craton (Hebei Province, China). Chem Geol 264:101–121

Cook NJ, Ciobanu CL, Meria D, Silcock D, Wade B (2013) Arsenopyrite-pyrite association in an orogenic gold ore: tracing mineralization history from textures and trace elements. Econ Geol 108:1273–1283

Costagliola P, Di Benedetto F, Benvenuti M, Bernardini GP, Cipriani C, Lattanzi PF, Romanelli M (2003) Chemical speciation of Ag in galena by EPR spectroscopy. Am Mineral 88:1345–1350

Danyushevsky L, Robinson P, Gilbert S, Norman M, Large R, McGoldrick P, Shelley M (2011) Routine quantitative multi-element analysis of sulphide minerals by laser ablation ICP-MS: standard development and consideration of matrix effects. Geochem: Explor Environ, Anal 11:51–60

Dong YP, Zhang GW, Neubauer F, Liu XM, Genser J, Hauzenberger C (2011) Tectonic evolution of the Qinling orogen, China: review and synthesis. J Asian Earth Sci 41:213–237

Fan WM, Zhang HF, Baker J, Jarvis KE, Mason P, Menzies MA (2000) On and off the North China Craton: where is the Archaean keel? J Petrol 41:933–950

Foord EE, Shawe DR (1989) The Pb–Bi–Ag–Cu–(Hg) chemistry of galena and some associated sulfosalts; a review and some new data from Colorado, California and Pennsylvania. Can Mineral 27:363

Foord EE, Shawe DR, Conklin NM (1988) Coexisting galena, PbSss and sulfosalts: evidence for multiple episodes of mineralization in the Round Mountain and Manhattan gold districts, Nevada. Can Mineral 26:355–376

Fougerouse D, Micklethwaite S, Halfpenny A, Reddy SM, Cliff JB, Martin LA, Kilburn M, Guagliardo P, Ulrich S (2016a) The golden ark: arsenopyrite crystal plasticity and the retention of gold through high strain and metamorphism. Terra Nova 28:181–187

Fougerouse D, Micklethwaite S, Tomkins AG, Mei Y, Kilburn M, Guagliardo P, Fisher LA, Halfpenny A, Gee M, Paterson D (2016b) Gold remobilisation and formation of high grade ore shoots driven by dissolution-reprecipitation replacement and Ni substitution into auriferous arsenopyrite. Geochim Cosmochim Acta 178:143–159

Fougerouse D, Reddy SM, Saxey DW, Rickard WD, van Riessen A, Micklethwaite S (2016c) Nanoscale gold clusters in arsenopyrite controlled by growth rate not concentration: evidence from atom probe microscopyk. Am Mineral 101:1916–1919

Gao XY, Zhao TP, Yuan ZL, Zhou YY, Gao JF (2010) Geochemistry and petrogenesis of the Heyu batholith in the southern margin of the North China block. Acta Petrol Sin 26:3485–3506 (in Chinese with English abstract)

Gao JJ, Mao JW, Chen MH, Ye HS, Zhang JJ, Li YF (2011) Vein structure analysis and $^{40}Ar/^{39}Ar$ dating of sericite from sub-ore altered rocks in the Tieluping large-size Ag–Pb deposit of western Henan province. Acta Geol Sinica 85:1172–1187 (in Chinese with English abstract)

Goldfarb RJ, Santosh M (2014) The dilemma of the Jiaodong gold deposits: are they unique? Geosci Front 5:139–153

Goldfarb RJ, Groves DI, Gardoll S (2001) Orogenic gold and geologic time: a global synthesis. Ore Geol Rev 18:1–75

Goldfarb RJ, Baker T, Dube B, Groves DI, Hart CJ, Gosselin P (2005) Distribution, character, and genesis of gold deposits in metamorphic terranes. Econ Geol 40:407–450

Groves DI (1993) The crustal continuum model for late-Archaean lode-gold deposits of the Yilgarn Block, Western Australia. Miner Depos 28:366–374

Groves DI, Ridley JR, Bloem E, Gebre-Mariam M, Hagemann SG, Hronsky J, Knight JT, McNaughton NJ, Ojala J, Vielreicher RM (1995) Lode-gold deposits of the Yilgarn block: products of Late Archaean crustal-scale overpressured hydrothermal systems. Geol Soc Lond Spec Publ 95:155–172

Groves DI, Goldfarb RJ, Gebre-Mariam M, Hagemann SG, Robert F (1998) Orogenic gold deposits: a proposed classification in the context of their crustal distribution and relationship to other gold deposit types. Ore Geol Rev 13:7–27

Groves DI, Goldfarb RJ, Robert F, Hart CJ (2003) Gold deposits in metamorphic belts: overview of current understanding, outstanding problems, future research, and exploration significance. Econ Geol 98:1–29

Guo B, Zhu LM, Li B, Gong HJ, Wang JQ (2009) Zircon U–Pb age and Hf isotope composition of the Huashan and Heyu granite plutons at the southern margin of North China Craton: implications for geodynamic setting. Acta Petrol Sin 25:265–281 (in Chinese with English abstract)

Hackbarth CJ, Petersen U (1984) A fractional crystallization model for the deposition of argentian tetrahedrite. Econ Geol 79:448–460

Harlov DE, Wirth R, Hetherington CJ (2011) Fluid-mediated partial alteration in monazite: the role of coupled dissolution-reprecipitation in element redistribution and mass transfer. Contrib Mineral Petrol 162:329–348

He YH, Zhao GC, Sun M, Xia XP (2009) SHRIMP and LA-ICP-MS zircon geochronology of the Xiong'er volcanic rocks: implications for the Paleo-Mesoproterozoic evolution of the southern margin of the North China Craton. Precambrian Res 168:213–222

Heinrich CA, Eadington PJ (1986) Thermodynamic predictions of the hydrothermal chemistry of arsenic, and their significance for the paragenetic sequence of some cassiterite-arsenopyrite-base metal sulfide deposits. Econ Geol 81:511–529

Hu SX, Lin QL, Chen ZM, Li SM (1988) Geology and metallogeny of the collision belt between the North and the South China plates. Nanjing University Press, Nanjing, 558 pp (in Chinese with English abstract)

Hu ZC, Zhang W, Liu YS, Gao S, Li M, Zong KQ, Chen HH, Hu SH (2014) "Wave" signal-smoothing and mercury-removing device for laser ablation quadrupole and multiple collector ICPMS analysis: application to lead isotope analysis. Anal Chem 87:1152–1157

Large RR, Maslennikov VV, Robert F, Danyushevsky LV, Chang Z (2007) Multistage sedimentary and metamorphic origin of pyrite and gold in the giant Sukhoi Log deposit, Lena gold province, Russia. Econ Geol 102:1233–1267

Large RR, Danyushevsky L, Hollit C, Maslennikov V, Meffre S, Gilbert S, Bull S, Scott R, Emsbo P, Thomas H (2009) Gold and trace element zonation in pyrite using a laser imaging technique: implications for the timing of gold in orogenic and Carlin-style sediment-hosted deposits. Econ Geol 104:635–668

Leach DL, Landis GP, Hofstra AH (1988) Metamorphic origin of the Coeur d'Alene base-and precious-metal veins in the Belt basin, Idaho and Montana. Geology 16:122–125

Leach DL, Hofstra AH, Church SE, Snee LW, Vaughn RB, Zartman RE (1998) Evidence for Proterozoic and Late Cretaceous-early Tertiary ore-forming events in the Coeur d'Alene District, Idaho and Montana. Econ Geol 93:347–359

Li SG, Xiao YL, Liu DL, Chen YZ, Sun SS, Hart SR, Wang SS (1993) Collision of North China and Yangtze blocks and formation of coesite-bearing eclogites: timing and processes. Chem Geol 109:89–111

Li YF, Mao JW, Bai FJ, Guo BJ, Wang ZG (2005) Precise Re-Os dating of molybdenite from the east Qinling molybdenum belt in central China and its geodynamic implications. In: Mao JW, Bierlein FP (eds) Proceedings of the eighth biennial SGA meeting. Springer, Beijing, pp 777–780

Li JW, Vasconcelos P, Zhou MF, Zhao XF, Ma CQ (2006) Geochronology of the Pengjiakuang and Rushan gold deposits, Eastern Jiaodong gold province, Northeastern China: implications for regional mineralization and geodynamic setting. Econ Geol 101:1023–1038

Li JW, Bi SJ, Selby D, Chen L, Vasconcelos P, Thiede D, Zhou MF, Zhao XF, Li ZK, Qiu HN (2012a) Giant Mesozoic gold provinces related to the destruction of the North China craton. Earth Planet Sci Lett 349:26–37

Li JW, Li ZK, Zhou MF, Chen L, Bi SJ, Deng XD, Qiu HN, Cohen B, Selby D, Zhao XF (2012b) The Early Cretaceous Yangzhaiyu lode gold deposit, North China Craton: a link between craton reactivation and gold veining. Econ Geol 107:43–79

Li ZK, Li JW, Zhao XF, Zhou MF, Selby D, Bi SJ, Sui JX, Zhao ZJ (2013) Crustal-extension Ag–Pb–Zn veins in the Xiong'ershan district, southern North China craton: constraints from the Shagou deposit. Econ Geol 108:1703–1729

Liu J, Davis GA, Lin Z, Wu F (2005) The Liaonan metamorphic core complex, Southeastern Liaoning Province, North China: a likely contributor to Cretaceous rotation of Eastern Liaoning, Korea and contiguous areas. Tectonophysics 407:65–80

Longerich HP, Jackson SE, Günther D (1996) Laser ablation inductively coupled plasma mass spectrometric transient signal data acquisition and analyte concentration calculation. J Anal At Spectrom 11:899–904

Lueth VW, Megaw P, Pingitore NE, Goodell PC (2000) Systematic variation in galena solid-solution compositions at Santa Eulalia, Chihuahua, Mexico. Econ Geol 95:1673–1687

Luo MJ, Li SM, Lu XX, Zheng DQ, Su ZB (2000) Metallogenesis and deposit series of main mineral resources of Henan Province. Geological Publishing House, Beijing, 355 pp (in Chinese with English abstract)

Lynch JVG (1989) Hydrothermal zoning in the Keno Hill Ag–Pb–Zn veins system, Yukon: A study in structural geology, mineralogy, fluid inclusions, and stable isotope geochemistry. Ph. D. thesis, University of Alberta, 190 pp

Mao JW, Goldfarb RJ, Zhang ZW, Xu WY, Qiu YM, Deng J (2002) Gold deposits in the Xiaoqinling-Xiong'ershan region, Qinling Mountains, central China. Miner Depos 37:306–325

Mao JW, Zheng RF, Ye HS, Gao JJ, Chen W (2006) ^{40}Ar/39 Ar dating of fuchsite and sericite from altered rocks close to ore veins in Shagou large-size Ag–Pb–Zn deposit of Xiong'ershan area, western Henan Province, and its significance. Miner Depos 25:359–368 (in Chinese with English abstract)

Mao JW, Xie GQ, Bierlein F, Qu WJ, Du AD, Ye HS, Pirajno F, Li HM, Guo BJ, Li YF (2008) Tectonic implications from Re–Os dating of Mesozoic molybdenum deposits in the East Qinling-Dabie orogenic belt. Geochim Cosmochim Acta 72:4607–4626

Mao JW, Xie GQ, Pirajno F, Ye HS, Wang YB, Li YF, Xiang JF, Zhao HJ (2010) Late Jurassic-Early Cretaceous granitoid magmatism in Eastern Qinling, central-eastern China: SHRIMP zircon U–Pb ages and tectonic implications. Aust J Earth Sci 57:51–78

Mavrogenes JA (2001) Partial melting of the Broken Hill Galena-Sphalerite ore: experimental studies in the system PbS-FeS-ZnS-(Ag2S). Econ Geol 96:205–210

McCuaig TC, Kerrich R (1998) "P–T–t"-deformation-fluid characteristics of lode gold deposits: evidence from alteration systematics. Ore Geol Rev 12:381–453

Menzies MA, Fan W, Zhang M (1993) Palaeozoic and Cenozoic lithoprobes and the loss of >120 km of Archaean lithosphere, Sino-Korean craton, China. Geol Soc Lond Spec Publ 76:71–81

Morey AA, Tomkins AG, Bierlein FP, Weinberg RF, Davidson GJ (2008) Bimodal distribution of gold in pyrite and arsenopyrite: examples from the Archean Boorara and Bardoc shear systems, Yilgarn Craton, Western Australia. Econ Geol 103:599–614

Müller W, Shelley M, Miller P, Broude S (2009) Initial performance metrics of a new custom-designed ArF excimer LA-ICPMS system coupled to a two-volume laser-ablation cell. J Anal At Spectrom 24:209–214

Mumin AH, Fleet ME, Chryssoulis SL (1994) Gold mineralization in As-rich mesothermal gold ores of the Bogosu-Prestea mining district of the Ashanti Gold Belt, Ghana: remobilization of "invisible" gold. Miner Depos 29:445–460

Oberthür T, Weiser T, Amanor JA, Chryssoulis SL (1997) Mineralogical siting and distribution of gold in quartz veins and sulfide ores of the Ashanti mine and other deposits in the Ashanti belt of Ghana: genetic implications. Miner Depos 32:2–15

Pals DW, Spry PG, Chryssoulis S (2003) Invisible gold and tellurium in arsenic-rich pyrite from the Emperor gold deposit, Fiji: implications for gold distribution and deposition. Econ Geol 98:479–493

Pei F, Xu W, Yang D, Yu Y, Wang W, Zhao Q (2011) Geochronology and geochemistry of Mesozoic mafic-ultramafic complexes in the southern Liaoning and southern Jilin provinces, NE China: constraints on the spatial extent of destruction of the North China Craton. J Asian Earth Sci 40:636–650

Peng P, Zhai M, Ernst RE, Guo J, Liu F, Hu B (2008) A 1.78 Ga large igneous province in the North China craton: the Xiong'er Volcanic Province and the North China dyke swarm. Lithos 101:260–280

Putnis A (2009) Mineral replacement reactions. Rev Mineral Geochem 70:87–124

Reddy SM, Hough RM (2013) Microstructural evolution and trace element mobility in Witwatersrand pyrite. Contrib Mineral Petrol 166:1269–1284

Reddy SM, Timms NE, Trimby P, Kinny PD, Buchan C, Blake K (2006) Crystal-plastic deformation of zircon: a defect in the assumption of chemical robustness. Geology 34:257–260

Reddy SM, Timms NE, Pantleon W, Trimby P (2007) Quantitative characterization of plastic deformation of zircon and geological implications. Contrib Mineral Petrol 153:625–645

Reich M, Kesler SE, Utsunomiya S, Palenik CS, Chryssoulis SL, Ewing RC (2005) Solubility of gold in arsenian pyrite. Geochim Cosmochim Acta 69:2781–2796

Ren J, Tamaki K, Li S, Junxia Z (2002) Late Mesozoic and Cenozoic rifting and its dynamic setting in Eastern China and adjacent areas. Tectonophysics 344:175–205

Sack RO, Kuehner SM, Hardy LS (2002) Retrograde Ag-enrichment in fahlores from the Coeur d'Alene mining district, Idaho, USA. Mineral Mag 66:215–229

Sack RO, Lynch J, Foit F (2003) Fahlore as a petrogenetic indicator: Keno Hill Ag–Pb–Zn district, Yukon, Canada. Mineral Mag 67:1023–1038

Sharp TG, Buseck PR (1993) The distribution of Ag and Sb in galena: inclusions versus solid solution. Am Mineral 78:85–95

Shi QZ, Wei XD, Li ML, Pang JQ (2004) Nappe and extensional detachment structures in north side of East Qinling, Henan. Geological Publishing House, Beijing, 204 pp (in Chinese with English abstract)

Stacey JT, Kramers JD (1975) Approximation of terrestrial lead isotope evolution by a two-stage model. Earth Planet Sci Lett 26:207–221

Stephenson PR, Fowler AP, Smith HA, Riles A (2014) Ying NI 43-101 technical report, Henan province. China AMC Mining Consultants (Canada) Ltd, Vancouver

Stevenson RK, Martin RF (1986) Implications of the presence of amazonite in the Broken Hill and Geco metamorphosed sulfide deposits. Can Mineral 24:729–745

Sung YH, Brugger J, Ciobanu CL, Pring A, Skinner W, Nugus M (2009) Invisible gold in arsenian pyrite and arsenopyrite from a multistage Archaean gold deposit: Sunrise Dam, Eastern Goldfields Province, Western Australia. Miner Depos 44:765–791

Tang KF (2014) Characteristics, genesis, and geodynamic setting of representative gold deposits in the Xiong'ershan district, southern margin of the North China Craton. Ph. D. thesis, China University of Geosciences (Wuhan), Wuhan, 162 pp (in Chinese with English abstract)

Tang KF, Li JW, Selby D, Zhou MF, Bi SJ, Deng XD (2013) Geology, mineralization, and geochronology of the Qianhe gold deposit, Xiong'ershan area, southern North China Craton. Miner Depos 48:729–747

Tian Z, Han P, Xu K (1992) The Mesozoic-Cenozoic east China rift system. Tectonophysics 208:341–363

Tomkins AG, Pattison DRM, Zaleski E (2004) The Hemlo Gold Deposit, Ontario: an Example of Melting and Mobilization of a Precious Metal-Sulfosalt Assemblage during Amphibolite Facies Metamorphism and Deformation. Econ Geol 99:1063–1084

Townsend AT, Yub Z, McGoldrickb P, Huttona JA (1998) Precise lead isotope ratios in Australian galena samples by high resolution inductively coupled plasma mass spectrometry. J Anal At Spectrom 13:809–813

Vaughan JP, Kyin A (2004) Refractory gold ores in Archaean greenstones, Western Australia: mineralogy, gold paragenesis, metallurgical characterization and classification. Mineral Mag 68:255–277

Velásquez G, Béziat D, Salvi S, Siebenaller L, Borisova AY, Pokrovski GS, De Parseval P (2014) Formation and deformation of pyrite and implications for gold mineralization in the El Callao District, Venezuela. Econ Geol 109:457–486

Voudouris PC, Spry PG, Sakellaris GA, Mavrogonatos C (2011) A cervelleite-like mineral and other Ag-Cu-Te-S minerals [Ag2CuTeS and (Ag, Cu)2TeS] in gold-bearing veins in metamorphic rocks of the Cycladic Blueschist Unit, Kallianou, Evia Island, Greece. Mineral Petrol 101:169–183

Vukmanovic Z, Reddy SM, Godel B, Barnes SJ, Fiorentini ML, Barnes SJ, Kilburn MR (2014) Relationship between microstructures and grain-scale trace element distribution in komatiite-hosted magmatic sulphide ores. Lithos 184–187:42–61

Wang ZG, Cui B, Xu ML (1997) the tectonic evolution and mineralization in the south the tectonic evolution and mineralization in the south region of north china block. Metallurgical Industry Press, Beijing, 310 pp (in Chinese with English abstract)

Wilson SA, Ridley WI, Koenig AE (2002) Development of sulfide calibration standards for the laser ablation inductively-coupled plasma mass spectrometry technique. J Anal At Spectrom 17:406–409

Woodhead J (2002) A simple method for obtaining highly accurate Pb isotope data by MC-ICP-MS. J Anal At Spectrom 17:1381–1385

Wu FY, Lin JQ, Wilde SA, Zhang XO, Yang JH (2005) Nature and significance of the Early Cretaceous giant igneous event in eastern China. Earth Planet Sci Lett 233:103–119

Yan JS, Wang MS, Yang JC, Xu YX (2000) Tectonic evolution of the Machaoying fault zone in western Henan and its relationship with Au polymetallic mineralization. Reg Geol China 19:166–171 (in Chinese with English abstract)

Yang ZY, Cheng YQ, Wang HZ (1986) The geology of China. Clarendon Press, Oxford, 306 pp

Yang JH, Wu FY, Wilde SA, Belousova E, Griffin WL (2008) Mesozoic decratonization of the North China block. Geology 36:467–470

Ye HS (2006) The Mesozoic tectonic evolution and Pb–Zn–Ag metallogeny in the south margin of North China Craton. Ph.D. thesis, China University of Geosciences, Beijing, 217 pp (in Chinese with English abstract)

Zeng N, Izawa E, Motomura Y, Lai L (2000) Silver minerals and paragenesis in the Kangjiawan Pb–Zn–Ag–Au deposit of the Shuikoushan mineral district, Hunan Province, China. Can Mineral 38:11–22

Zhang JJ, Zheng YD (1999) The multiphase extension and their ages of the Xiaoqinling metamorphic core complex. Acta Geol Sinica 73:139–147 (in Chinese with English abstract)

Zhao GC, Wilde SA, Cawood PA, Sun M (2001) Archean blocks and their boundaries in the North China Craton: lithological, geochemical, structural and P–T path constraints and tectonic evolution. Precambrian Res 107:45–73

Zhao TP, Zhou MF, Zhai M, Xia B (2002) Paleoproterozoic rift-related volcanism of the Xiong'er Group, North China Craton: implications for the breakup of Columbia. Int Geol Rev 44:336–351

Zhao TP, Zhai MG, Xia B, Li HM, Zhang YX, Wan YS (2004) Zircon U–Pb SHRIMP dating for the volcanic rocks of the Xiong'er Group: constraints on the initial formation age of the cover of the North China Craton. Chin Sci Bull 49:2495–2502

Zheng YD, Wang SZ, Wang YF (1991) An enormous thrust nappe and extensional metamorphic core complex newly discovered in Sino-Mongolian boundary area. Sci China B 34:1145–1154

Zhu G, Niu M, Xie C, Wang Y (2010) Sinistral to normal faulting along the Tan-Lu Fault Zone: evidence for geodynamic switching of the East China continental margin. J Geol 118:277–293

Zhu RX, Yang JH, Wu FY (2012) Timing of destruction of the North China Craton. Lithos 149:51–60

Zhu RX, Fan HR, Li JW, Meng QR, Li SR, Zeng QD (2015) Decratonic gold deposits. Sci China Earth Sci 58:1523–1537

Acknowledgments

We acknowledge the financial support from the Ministry of Science and Technology of China (2016YFC0600104) and Natural Science Foundation of China (91514303, 41402066, 41325007, 91414301). David Cooke, Leonid Danyushevsky and Lejun Zhang acknowledge the financial support of the Australian Research Council through the Industrial Transformation Research Hub grant and Center of Excellence Funding Programs. This is a Finnish Geosciences Research Laboratory (SGL) contribution. Hong-Wei Qiao and Hao-Ran Zhang of Henan Found Mining Ltd. and Ji-Xiang Sui and Ke-Fei Tang from China University of Geosciences (Wuhan) provided logistic help during the field work. We are indebted to Sarah Gilbert and Jay Thompson for assistance with LA-ICPMS analyses at CODES, University of Tasmania. The manuscript benefitted significantly from careful reviews by Dr. Alan Boyle and Dr. Denis Fougerouse. Our thanks extend to Associate Editor Prof. Steven Reddy for editorial handling.

Fig. 1 Geological map showing major mineral districts along the southern margin of the North China Craton (modified from Mao et al. 2010). Inset indicates tectonic location of the southern North China Craton in East China. For more details see text. MCC metamorphic core complex

Fig. 2 Geological map of the Haopinggou deposit in the Xiayu ore field (simplified from Nonferrous Metals Geological Survey of Henan Province, unpublished data, 2003). For location of the map see Fig. 1

Fig. 3 Photographs (a–c) and reflected light photomicrographs (d–f) showing structures, textures, and mineralogy of Stage 1 pyrite–quartz veins and Stage 2 Pb–Zn-sulfide veins at Haopinggou. a Polymetallic sulfide vein as fracture infillings. The marginal pyrite–quartz vein was intruded by the Pb–Zn-sulfide vein and enclosed by intensive hydrothermal alteration. Note the pyrite–quartz vein was deformed. b Pb– Zn-sulfide veins crosscutting the pyrite–quartz vein. Note that foliation and banded structures are well developed in the pyrite–quartz vein and Pb–Zn-sulfide vein, respectively. c Fragments of pyrite–quartz veins included in the Pb–Zn-sulfide vein. d Stage 1 coarse-grained pyrite aggregates have abundant microfractures with a preferred orientation. The microfractures are locally filled with chalcopyrite. Siderite is the major gangue minerals intergrown with pyrite. Position of Fig. 7a is indicated. e Massive Stage 2 galena replacing coarse-grained pyrite in Stage 1 pyrite–quartz vein. Note that the pyrite contains abundant galena inclusions. f Quartz-ankerite vein crosscutting Pb– Zn-sulfide assemblages at Stage 2. Py pyrite, Qz quartz, Sp sphalerite, Gn galena, Cal calcite, Sd siderite, Ccp chalcopyrite, Ank ankerite

Fig. 4 Reflected light photomicrographs (a–d) and back-scattered electron images (e–f) showing occurrences and textural features of gold minerals from Stage 1 pyrite–quartz veins. a Native gold forming irregular grains in siderite and magnetite. Minor galena inclusions occur in magnetite. b Native gold and electrum present in siderite as inclusions. Magnetite, arsenopyrite, and galena also occur in siderite. c Irregular electrum grains in pyrite, magnetite, and galena. Chalcopyrite and galena replacing magnetite and pyrite; all these metallic minerals are altered by siderite and quartz. d Electrum grains in pyrite or between pyrite and quartz. e Irregular electrum and kustelite grains or stringers in siderite. Minor pyrite and quartz also occur in siderite. f Kustelite grains intergrown with pyrite in siderite. Abbreviations as in Table 1

Fig. 5 Reflected light photomicrographs (a–d) and back-scattered electron images (e–f) showing occurrences and textural features of silver minerals from Stage 2 Pb–Zn-sulfide veins. a Tetrahedrite and polybasite intergrown with galena, all replacing chalcopyrite. b Argentiferous tetrahedrite, stromeyerite, chalcopyrite, and quartz forming a vein filling sphalerite. Chalcopyrite is present as inclusions in sphalerite. c Argentiferous tetrahedrite, polybasite, and pyrargyrite intergrown with chalcopyrite, all included in galena. d Polybasite and pyrargyrite intergrown with sphalerite in galena. e Polybasite and argentite replacing chalcopyrite in quartz. Polybasite is surrounded by argentite. f Aggregates of argentiferous tetrahedrite, argentite and native silver in chalcopyrite. Abbreviations as in Table 1

Fig. 6 Reflected light photomicrographs (a, c–e) and back-scattered electron images (b, f) showing three generations of pyrite from the Stage 1 pyrite–quartz vein (Py1 to Py3; a–c) and Stage 2 Pb–Znsulfide (Py4 to Py6; d–f). See text for more details. Pyrite grains in a, d, and e were etched with nitric acid to reveal growth zonation patterns. Abbreviations as in Table 1

Fig. 7 Results of EBSD analysis of selected pyrite grains in Stage 1 (a–d from sample HP32; e–h from sample HP41). a Reflected light photomicrograph showing oriented microfractures (dashed red arrows) in pyrite aggregates. Note that siderite veins and chalcopyrite inclusions (red arrows) are

present mainly in the microfractures. Circled red line refers to pyrite grains imaged in c. b Orientation contrast image (OCI) showing the variation of lattice orientation in different pyrite grains. c Colored EBSD image showing crystallographic misorientations of selected pyrite grains in the range of 0°–15°. The initial "reference" orientation point is marked as a red cross on the grain. d Scattered pole figures for pyrites in c suggesting an apparent

anticlockwise rotation around one [100] axis. Rotation direction is marked by black arrow. e Reflected light photomicrographs showing a pyrite aggregate. Inclusions of galena (black arrows) and chalcopyrite (red arrows) occurring mainly in intergrainular boundaries and microfractures of pyrite grains. Position of a pyrite grain in f and g is marked by circled red curves. f Euler orientation image showing the aggregate is composed of seven pyrite grains with different colors. g Colored EBSD image showing slight crystallographic misorientations (0°–4°) in selected pyrite grain. The initial "reference" orientation point is marked as a red cross. h Scattered pole figures for the seven measured pyrite grains in f. Abbreviations as in Table 1

Fig. 8 Diagrams showing the concentrations of selected trace elements in different generations (a–d) and stages (e) of pyrite. a–b Ranges of content (a) and comparisons of mean content (b) of trace elements in Py1 to Py3 from the pyrite–quartz stage. c–d Ranges of concentrations (c) and comparisons of mean concentrations (d) of trace elements in Py4 to Py6 from the Pb–Zn-sulfide stage. Red dotted line indicates the detection limits of the trace elements. e Spidergram showing the average concentrations of trace elements of three pyrite generations in Stage 1 and Stage 2. Pyrites from Stage 1 and Stage 2 are enriched in Au, As, Co, Ni, Bi and Ag, Pb, Zn, Sn, Sb, respectively

Fig. 9 Representative LA-ICPMS time-resolved spectra for pyrite grains of different generations at Haopinggou. a Py1; note the relative high counts of Pb, As, Bi, Sb, Zn, Cu, and Ag, and low counts of Au. b Py2; high counts of As and Au. Note the profiles for As and Au are parallel with that for Fe. c Py3; note the profiles for most elements are unstable except the profile for As. The spikes both in the profiles for Au and Ag indicate microinclusions of Au–Ag compounds. d Py4; note the relative high counts of As, Cu, Zn, Ag, Sb, and Pb and the fact that the profiles for these elements are mostly parallel. e Py5; note the high counts of As, whereas the counts for other elements are quite low. f Py6; note the extremely high counts of Pb, followed by Ag, Sb, etc

Fig. 10 LA-ICPMS images with logarithmic color scales (in ppm) showing contents and distribution patterns of trace elements of pyrite from Stage 1 (a from sample HP41; b from sample 32). a The same pyrite aggregate as in Fig. 7e. The boundaries of three large grains are highlighted by red line, with one grain consisting of three generations of pyrite (Py1, Py2, Py3). Note that gold nanoparticles occur in grain boundary. b A pyrite grain consists of two generations of pyrite. The core (Py 1) is enriched in inclusions of galena (red arrows) and chalcopyrite (black arrows), whereas the overgrowth (Py2) is free of inclusions. Note that the pyrite grains are penetrated by microfractures (red dashed lines) which are filled with chalcopyrite veins and gold nanoparticles. See text for more explanations

Fig. 11 LA-ICPMS images with logarithmic color scales (in ppm) showing trace element contents of pyrite from Stage 2 (sample HP46). This grain consists of two generations of pyrite (Py4, Py5). More textural details of this pyrite grain are shown in Fig. 6d. See text for more explanations

Fig. 12 Binary plots of selected trace elements in different generations of pyrite at Haopinggou. The solid and dotted lines in a, b represent the compositional trend of pyrite from Stage 1 pyrite–quartz vein and Stage 2 Pb–Zn-sulfide vein, respectively. The shaded areas show the average detection limits of the trace elements. a Gold and silver in pyrite from both assemblages are broadly correlated

positively. Note that pyrite from Stage 1 quartz-pyrite veins is enriched in Au, whereas pyrite from Stage 2 Pb–Zn-sulfide veins contains much higher Ag. b Au versus As plot showing several spot analyses from Py3 plot above the Au saturation line (Reich et al. 2005), indicating microinclusions of native gold contained in pyrite. The remaining analyses below this line are consistent with the predominance of invisible gold within the pyrite, particularly in Py2 and Py3. c A positive correlation between Pb and Ag indicates that Ag may be contained in galena inclusions in pyrite grains. d Silver and Sb are positively correlated in pyrite from the Pb–Zn-sulfide veins, indicating that both Ag and Sb are hosted in galena inclusions or occur as Ag–Sb-sulfosalt inclusions in pyrite. Such a correlation, however, is not observed for pyrite from the pyrite–quartz veins

Fig. 13 Back-scattered electron images showing silver minerals in galena at Haopinggou. a Tetrahedrite and argentiferous tetrahedrite as inclusions in galena. b Stringers of argentiferous tetrahedrite and polybasite in galena. Abbreviations as in Table 1

Fig. 14 In situ LA-ICPMS analyses of $^{207}Pb/^{204}Pb$ and $^{206}Pb/^{204}Pb$ on galena and pyrite from Stage 1 and Stage 2 at Haopinggou. The diameters for spots on galena and pyrite are 5 and 44 μm, respectively. The model Pb curve (μ = 9.74) is from Stacey and Kramers (1975). Data from Stage 1 and Stage 2 plot in completely separate areas of this diagram; however, they are both seated on the Pb curve with μ = 9.4. The shaded area indicates the Pb isotopic compositions of feldspar from the Haopinggou porphyry (Wang et al. 1997). Abbreviations as in Table 1

Fig. 15 Schematic diagram showing formation and evolution of various pyrite generations from Stage 1 pyrite–quartz veins (a) and Stage 2 Pb–Zn-sulfide veins (b). a Auriferous fluids initially migrated into the faults and deposited the early pyrite–quartz veins containing three generations of pyrite (Py1, Py2, and Py3). Py1 is coarse-grained and contains clusters of very fine-grained inclusions (e.g., sulfides) that likely explain the enrichment of a variety of trace elements such as Ag, Pb, Cu, Ni, Sb, and Bi in the pyrite. Py2 typically occurs as overgrowths of Py1 and rarely contains mineral inclusions. Trace elements are generally depleted in Py2, with the exceptions of As and Au. Py3 occurs as selvages enclosing the earlier formed pyrite or as microfracture fillings in the earlier pyrite. The Py3 contains abundant mineral inclusions, particularly native gold and electrum and has high contents of a large number of trace elements such as Au, Ag, As, Co, Pb, Zn, Cu, Sb, and Bi. b In an independent mineralizing event, Ag-rich fluids were introduced into the same fault systems and deposited the Pb–Zn-sulfide veins that overprinted or crosscut the earlier pyrite–quartz veins. The Pb–Zn-sulfide veins consist of three generations of pyrite, namely Py4, Py5, and Py6. Py4 contains abundant mineral inclusions and is enriched in Ag, Sb, Cu, Pb, Co, and Ni. In contrast, Py5, enclosing Py4, is depleted in most of these trace elements with the exceptions of As and Au. Py6 contains a variety of mineral inclusions dominated by Pb–Zn-sulfides, indicating that the formation of Py6 was coeval with the Ag–Pb–Zn mineralization. In addition, Py6 has high contents of Ag and Sb, most likely due to the presence of galena inclusions as Ag can be incorporated into the lattices of galena together with Sb by substitution for Pb. Meanwhile, a variety of silver minerals with close relationships with galena formed through Ag–Cu solid-state exchange reaction (Sack et al. 2002, 2003) or by Ag exsolution from the galena due to temperature decrease (Sharp and Buseck 1993; Chutas et al. 2008)

Table 1 Locations and descriptions of samples used for this study

Table 2 Electron microprobe data of gold and silver minerals from Haopinggou deposit

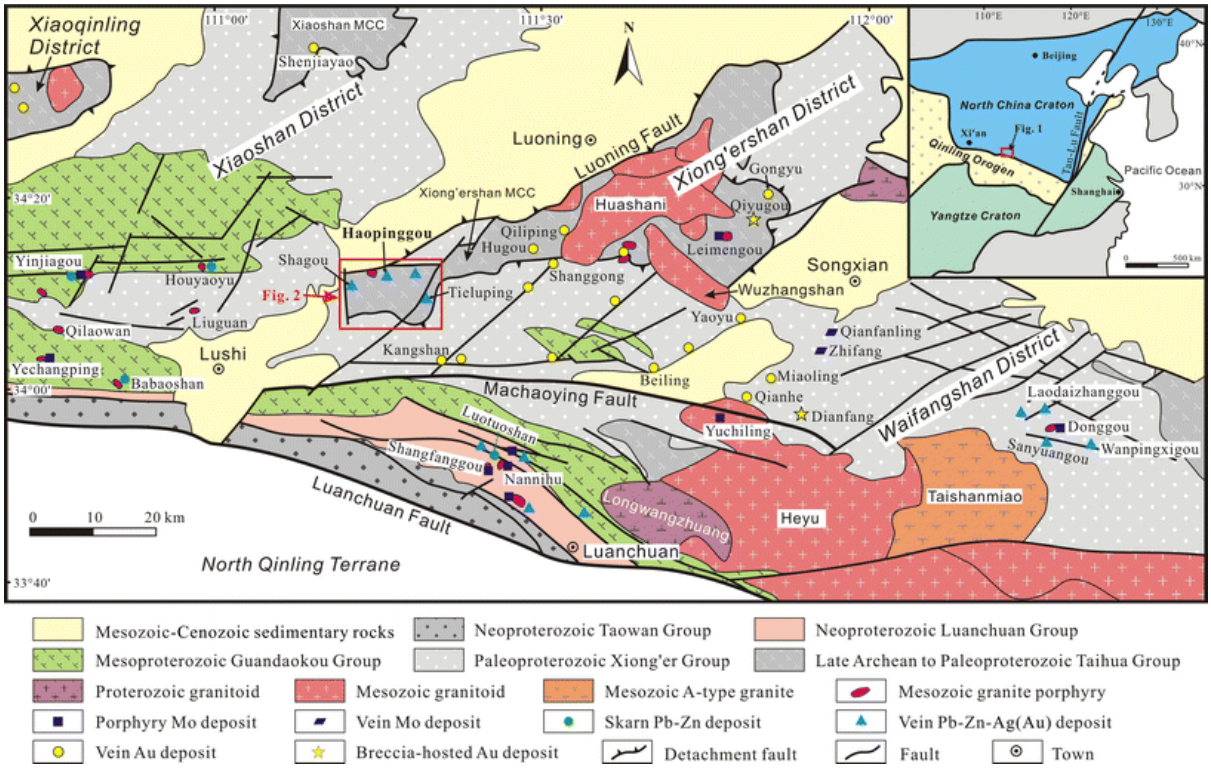
Xiaoqinling District
Xiaoshan District
Xiong'ershan District
Waifangshan District
Luoning
Luoning Fault
Machaoying Fault
Luanchuan Fault
North Qinling Terrane
Xiaoshan MCC
Xiong'ershan MCC
Shenjiayao
Haopinggou
Huashani
Gongyu
Qiyugou
Leimengou
Qiliping
Hugou
Shagou
Yinjiagou
Houyaoyu
Liuguan
Qilaowan
Yechangping
Babaoshan
Lushi
Fig. 2
Tieluping
Shanggong
Songxian
Wuzhangshan
Yaoyu
Qianfanling
Zhifang
Miaoling
Qianhe
Dianfang
Beiling
Kangshan
Yuchiling
Laodaizhanggou
Donggou
Sanyuangou
Wanpingxigou
Luotuoshan
Shangfanggou
Nannihu
Longwangzhuang
Heyu
Taishanmiao
Luanchuan
0 10 20 km
111°00'
111°30'
112°00'
34°20'
34°00'
33°40'
N
110°E
120°E
130°E
40°N
30°N
Beijing
North China Craton
Xi'an
Fig. 1
Qinling Orogen
Tan-Lu Fault
Pacific Ocean
Shanghai
Yangtze Craton
0 500 km
Mesozoic-Cenozoic sedimentary rocks
Neoproterozoic Taowan Group
Neoproterozoic Luanchuan Group
Mesoproterozoic Guandaokou Group
Paleoproterozoic Xiong'er Group
Late Archean to Paleoproterozoic Taihua Group
Proterozoic granitoid
Mesozoic granitoid
Mesozoic A-type granite
Mesozoic granite porphyry
Porphyry Mo deposit
Vein Mo deposit
Skarn Pb-Zn deposit
Vein Pb-Zn-Ag(Au) deposit
Vein Au deposit
Breccia-hosted Au deposit
Detachment fault
Fault
Town

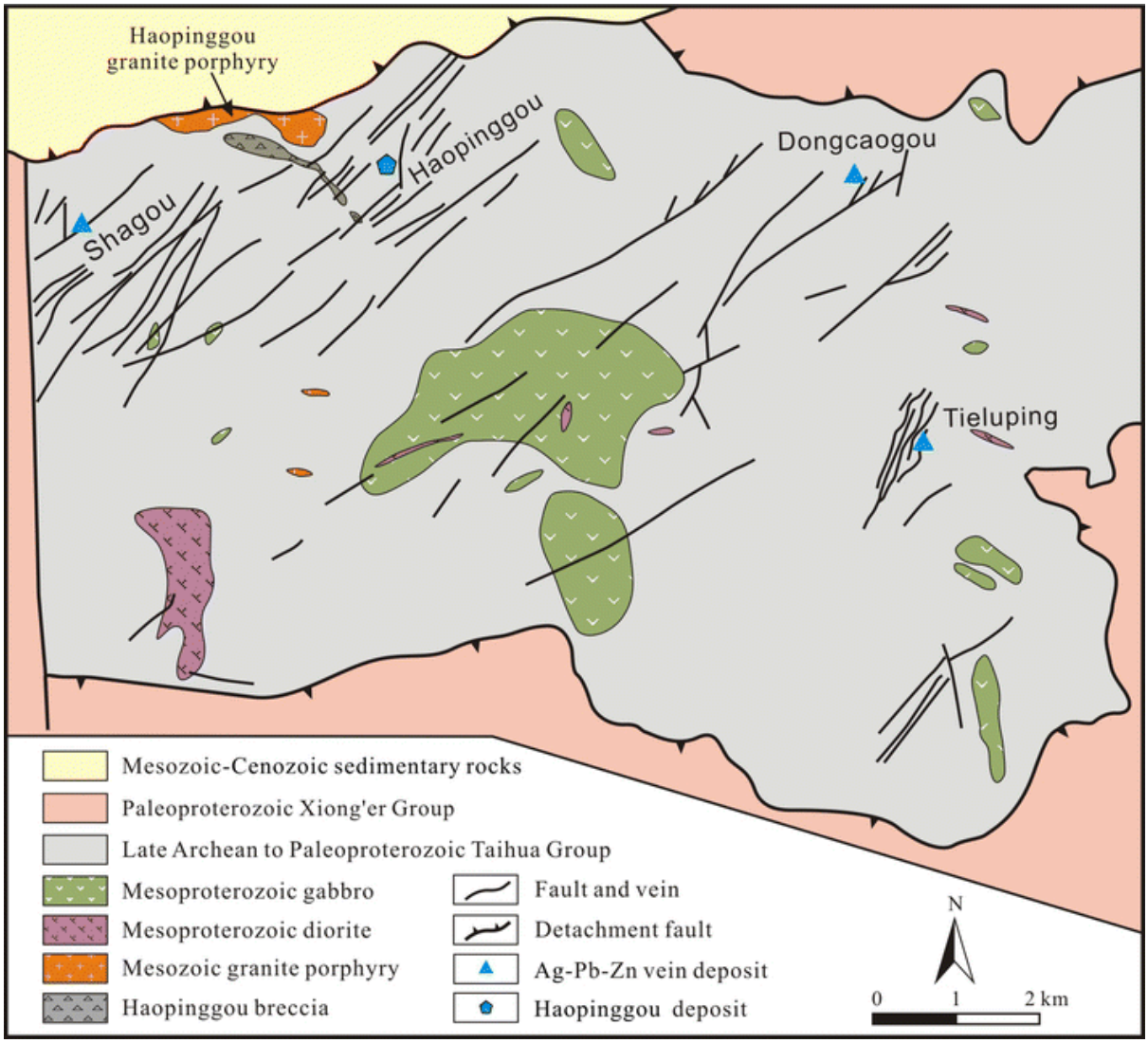
Haopinggou
granite porphyry
Haopinggou
Shagou
Dongcaogou
Tieluping
Mesozoic-Cenozoic sedimentary rocks
Paleoproterozoic Xiong'er Group
Late Archean to Paleoproterozoic Taihua Group
Mesoproterozoic gabbro
Mesoproterozoic diorite
Mesozoic granite porphyry
Haopinggou breccia
Fault and vein
Detachment fault
Ag-Pb-Zn vein deposit
Haopinggou deposit
N
0
1
2 km

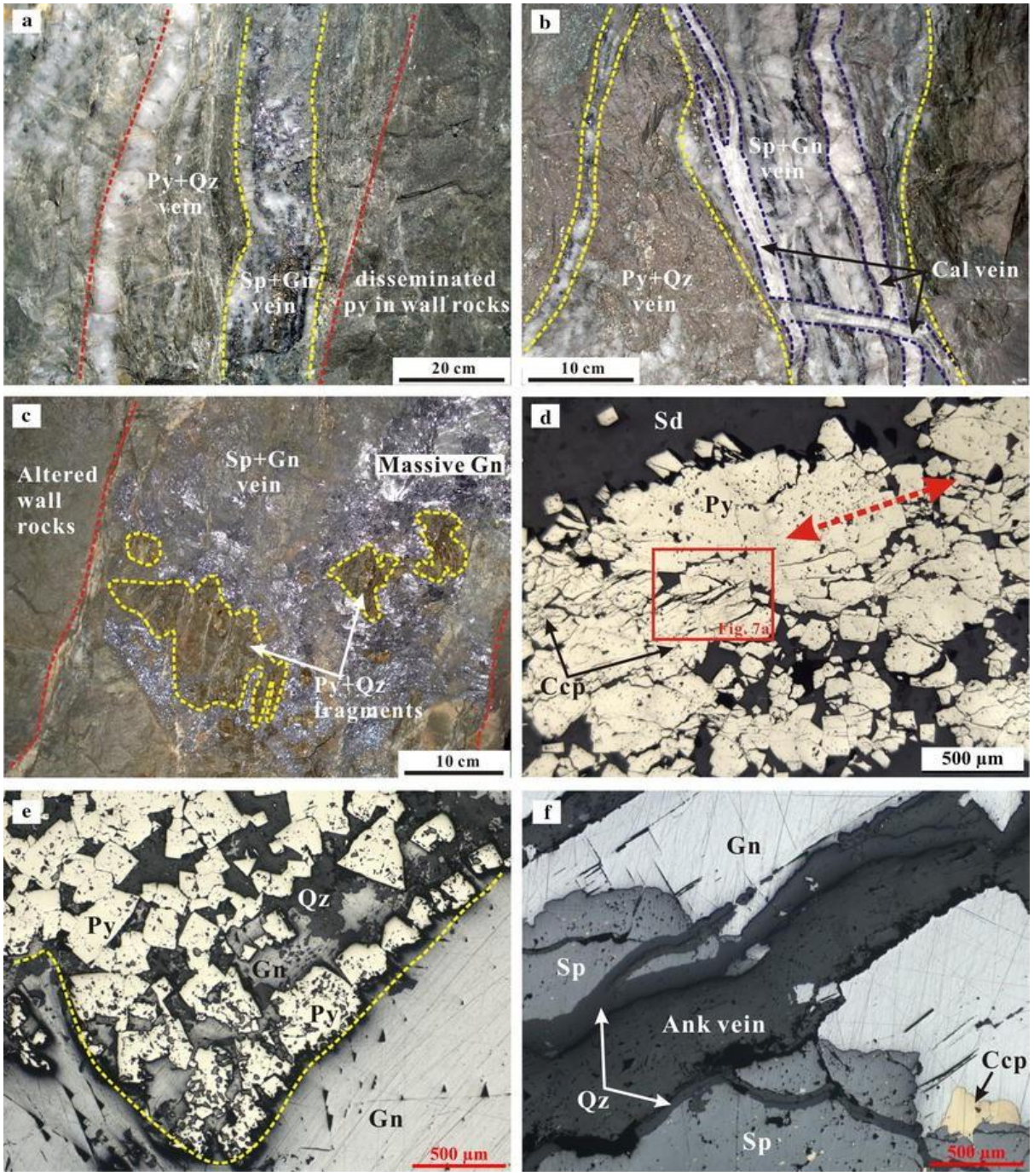
a
Py+Qz vein
Sp+Gn vein
disseminated py in wall rocks
20 cm
b
Sp+Gn vein
Cal vein
Py+Qz vein
10 cm
c
Altered wall rocks
Sp+Gn vein
Massive Gn
Py+Qz fragments
10 cm
d
Sd
Py
Fig. 7a
Ccp
500 μm
e
Py
Qz
Gn
Py
Gn
500 μm
f
Gn
Sp
Ank vein
Qz
Ccp
Sp
500 μm

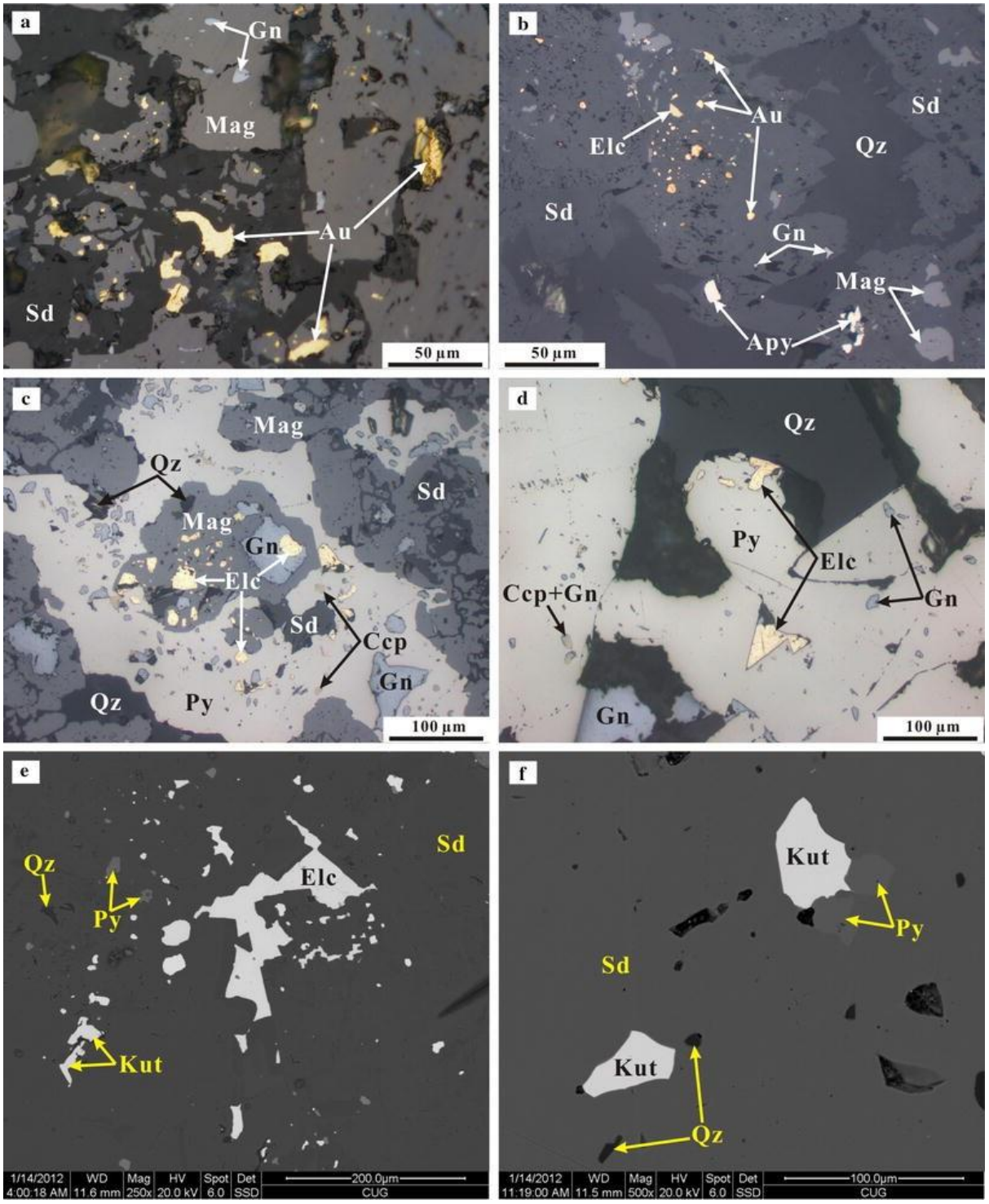
a
Gn
Mag
Au
Sd
50 μm
b
Au
Sd
Elc
Qz
Sd
Gn
Mag
Apy
50 μm
c
Mag
Qz
Sd
Mag
Gn
Elc
Sd
Ccp
Gn
Qz
Py
100 μm
d
Qz
Py
Elc
Ccp+Gn
Gn
Gn
100 μm
e
Qz
Sd
Elc
Py
Kut
1/14/2012 4:00:18 AM
WD 11.6 mm
Mag 250x
HV 20.0 kV
Spot 6.0
Det SSD
200.0μm
CUG
f
Kut
Py
Sd
Kut
Qz
1/14/2012 11:19:00 AM
WD 11.5 mm
Mag 500x
HV 20.0 kV
Spot 6.0
Det SSD
100.0μm
CUG

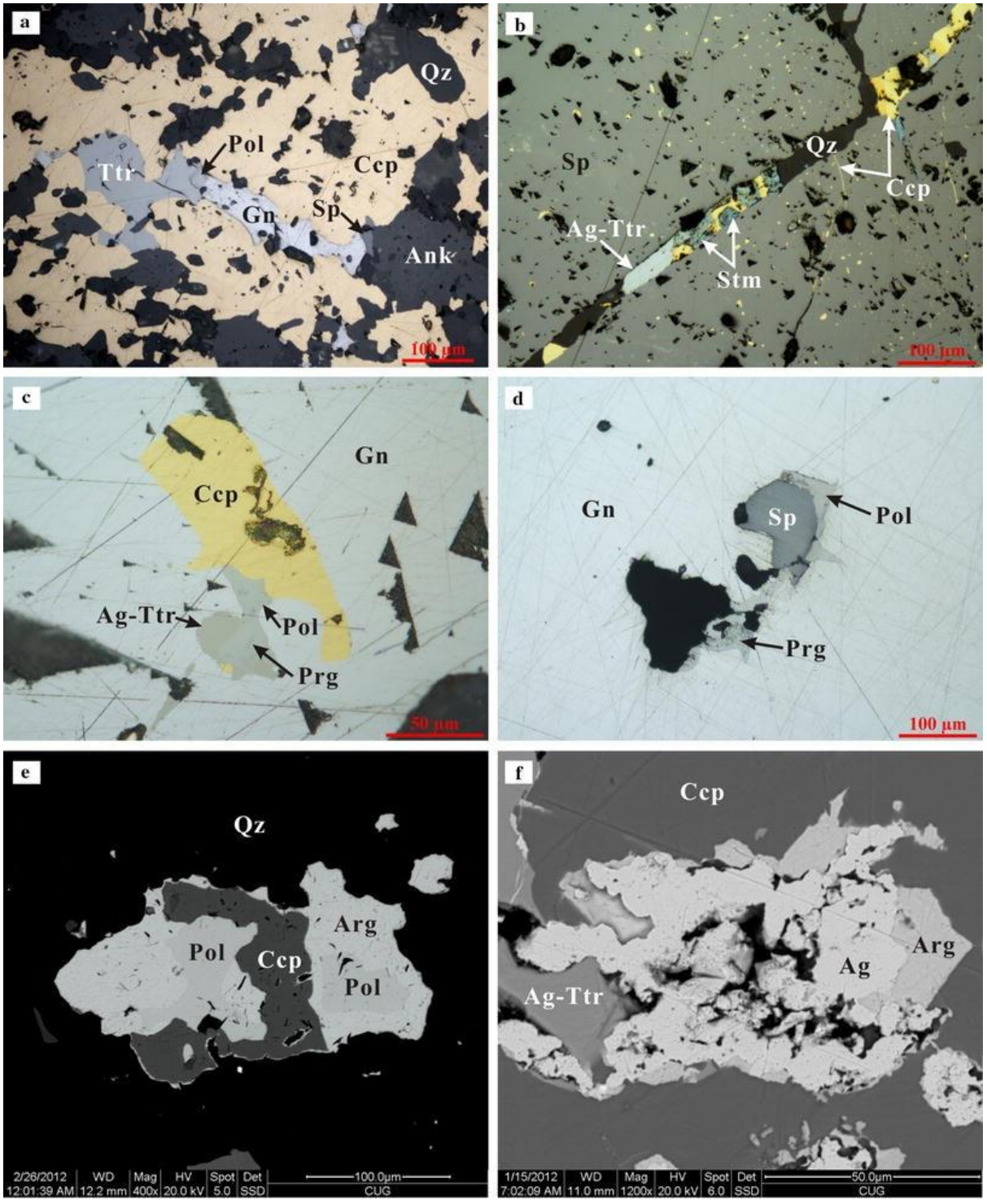
a
Qz
Pol
Ttr
Ccp
Gn
Sp
Ank
100 µm
b
Sp
Qz
Ccp
Ag-Ttr
Stm
100 µm
c
Gn
Ccp
Ag-Ttr
Pol
Prg
50 µm
d
Gn
Sp
Pol
Prg
100 µm
e
Qz
Arg
Pol
Ccp
Pol
2/26/2012 12:01:39 AM | WD 12.2 mm | Mag 400x | HV 20.0 kV | Spot 5.0 | Det SSD | 100.0µm | CUG
f
Ccp
Arg
Ag
Ag-Ttr
1/15/2012 7:02:09 AM | WD 11.0 mm | Mag 1200x | HV 20.0 kV | Spot 6.0 | Det SSD | 50.0µm | CUG

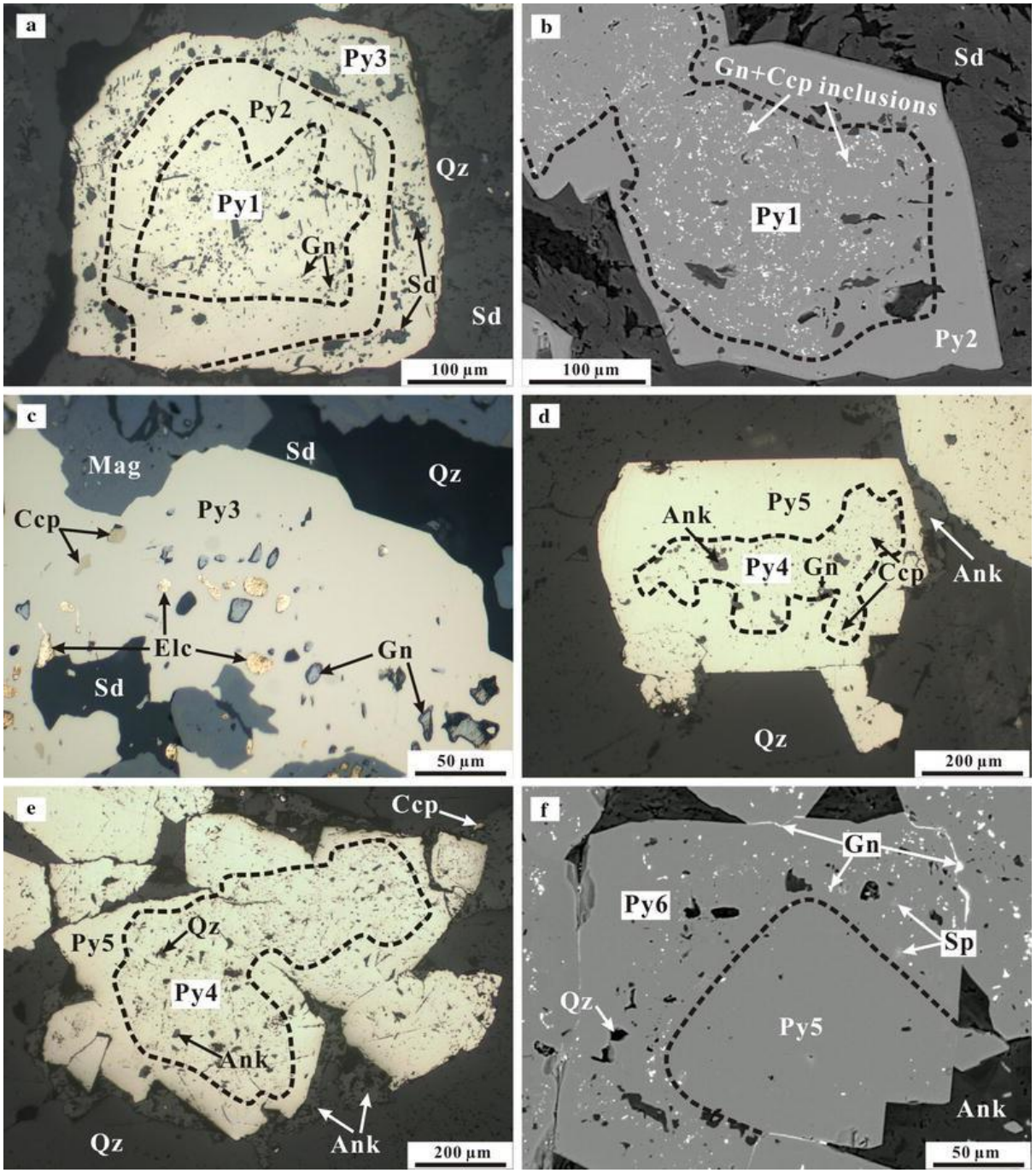
a
Py3
Py2
Py1
Qz
Gn
Sd
Sd
100 μm
b
Sd
Gn+Ccp inclusions
Py1
Py2
100 μm
c
Mag
Sd
Qz
Ccp
Py3
Elc
Gn
Sd
50 μm
d
Ank
Py5
Py4
Gn
Ccp
Ank
Qz
200 μm
e
Ccp
Qz
Py5
Py4
Ank
Qz
Ank
200 μm
f
Gn
Py6
Sp
Qz
Py5
Ank
50 μm

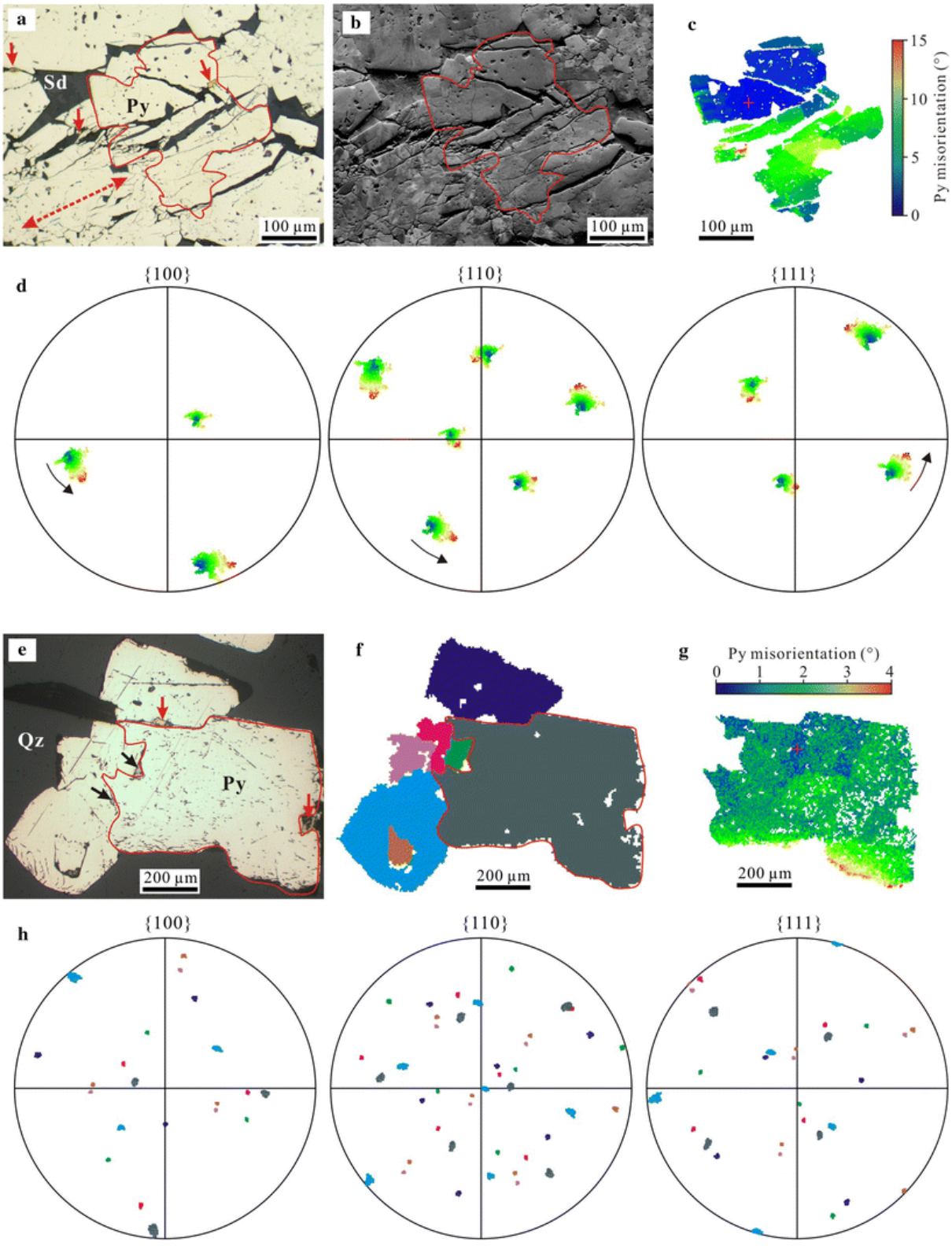
a
Sd
Py
100 µm
b
100 µm
c
100 µm
15
10
5
0
Py misorientation (°)
d
{100}
{110}
{111}
e
Qz
Py
200 µm
f
200 µm
g
Py misorientation (°)
0 1 2 3 4
200 µm
h
{100}
{110}
{111}

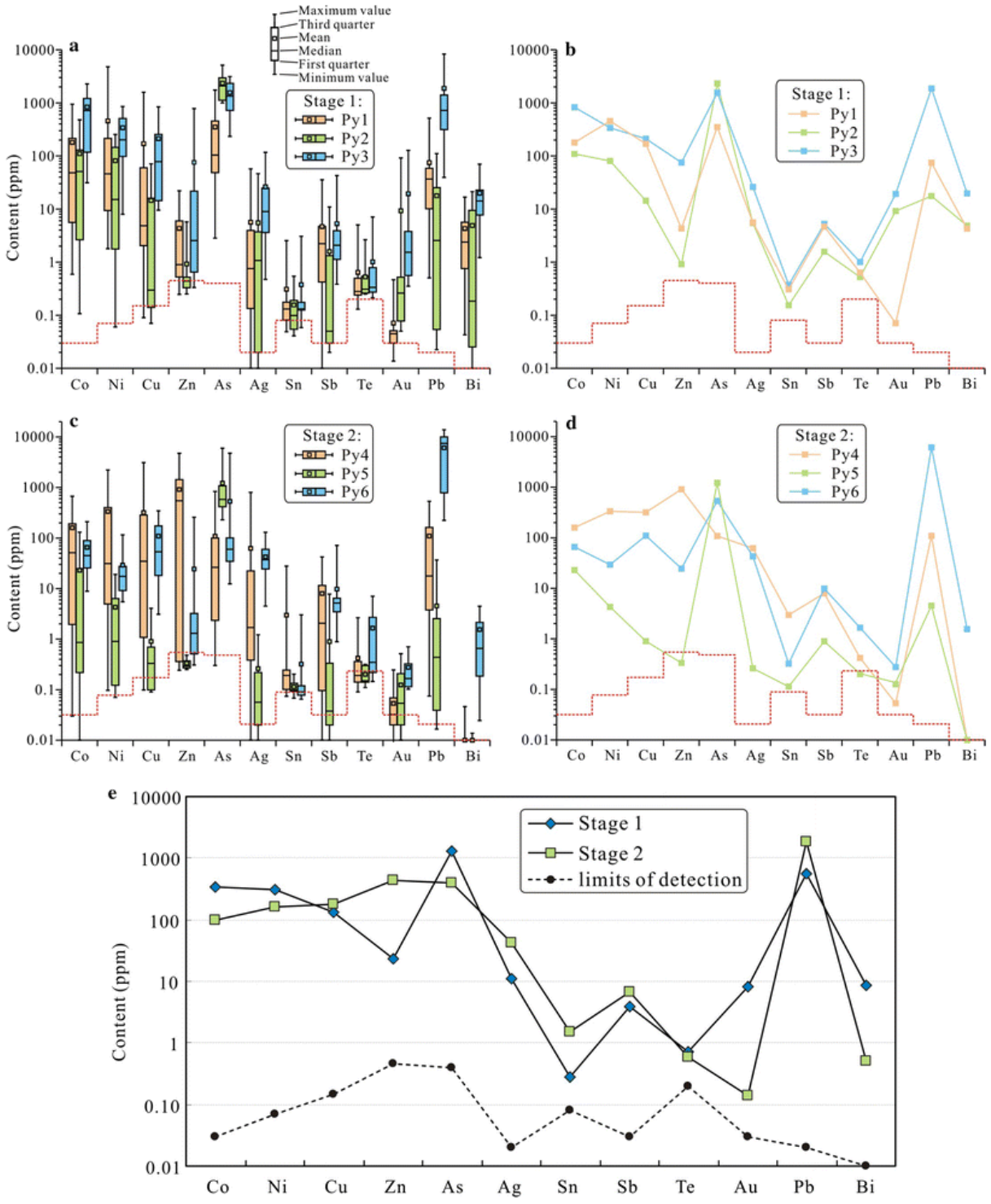
a
Maximum value
Third quarter
Mean
Median
First quarter
Minimum value
Stage 1:
Py1
Py2
Py3
Content (ppm)
10000
1000
100
10
1
0.1
0.01
Co Ni Cu Zn As Ag Sn Sb Te Au Pb Bi
b
Stage 1:
Py1
Py2
Py3
c
Stage 2:
Py4
Py5
Py6
d
Stage 2:
Py4
Py5
Py6
e
Stage 1
Stage 2
limits of detection

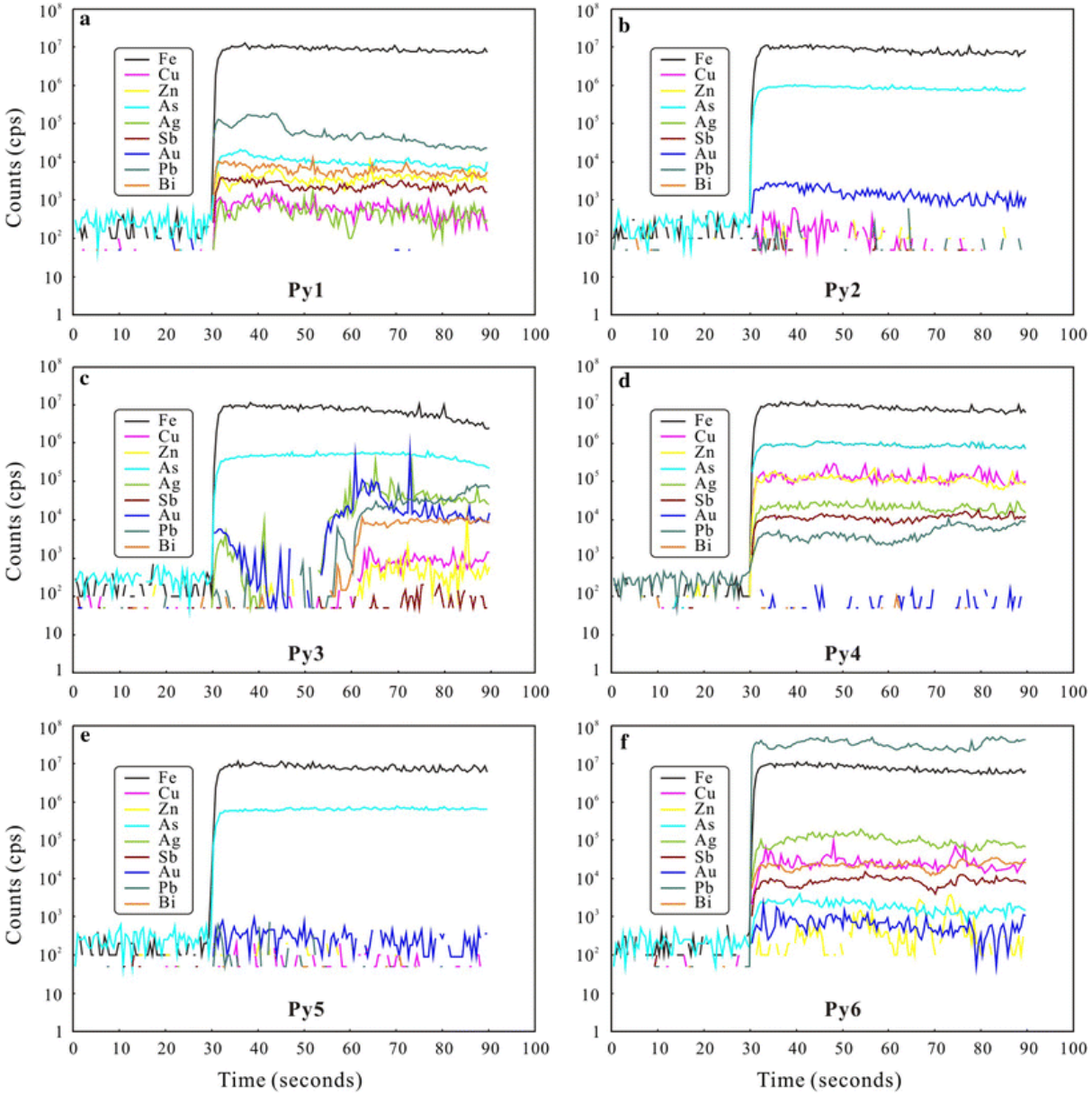
a
b
c
d
e
f
Fe
Cu
Zn
As
Ag
Sb
Au
Pb
Bi
Py1
Py2
Py3
Py4
Py5
Py6
Counts (cps)
Time (seconds)

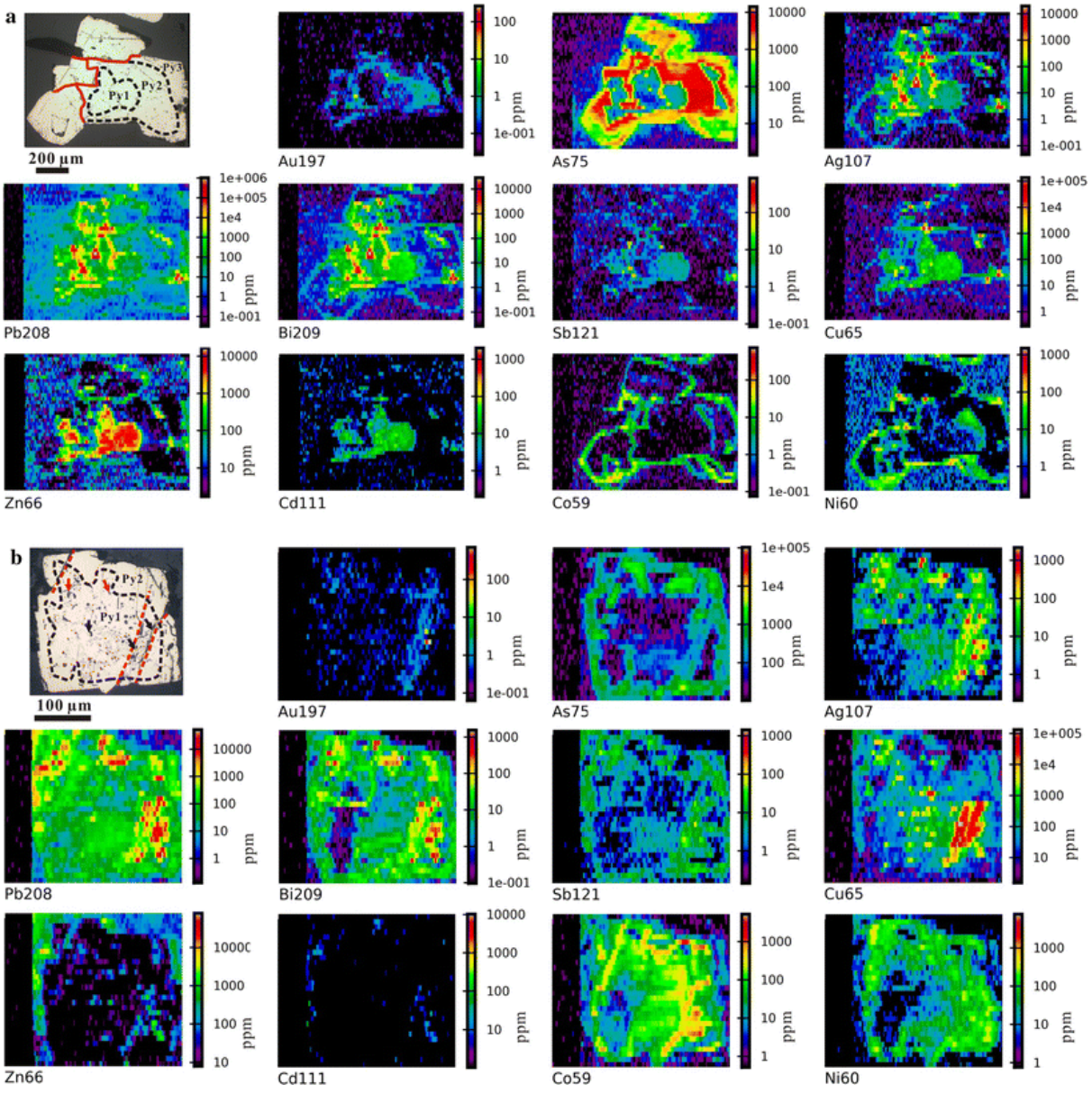
a
Py3
Py2
Py1
200 µm
Au197
As75
Ag107
Pb208
Bi209
Sb121
Cu65
Zn66
Cd111
Co59
Ni60
ppm
b
Py2
Py1
100 µm
Au197
As75
Ag107
Pb208
Bi209
Sb121
Cu65
Zn66
Cd111
Co59
Ni60
ppm

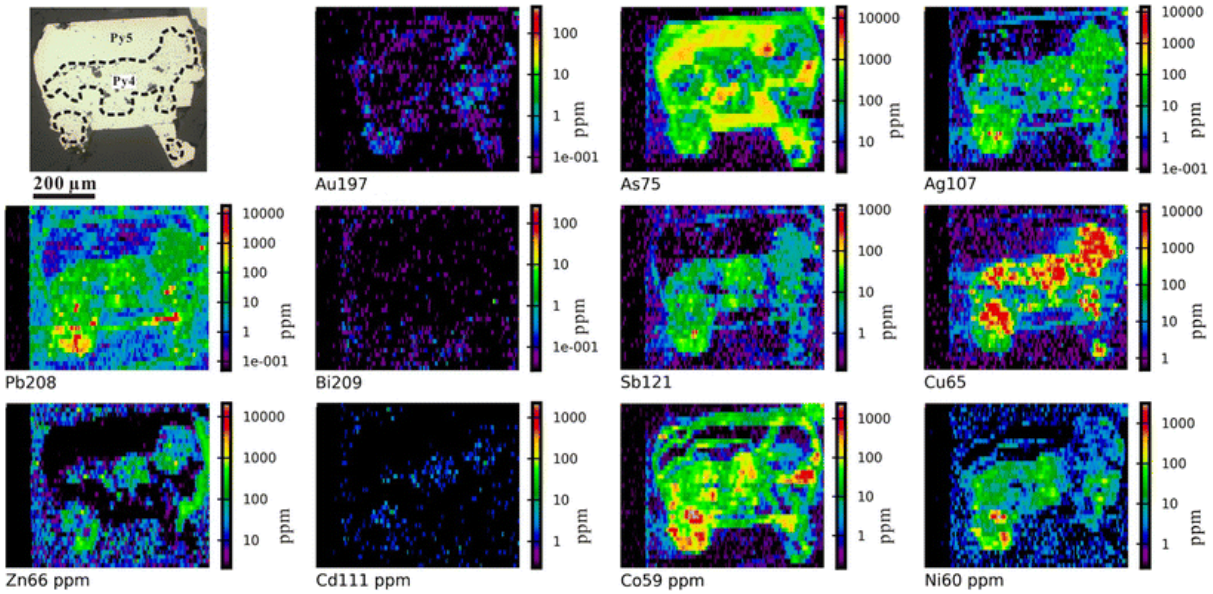
Py5
Py4
200 µm
Au197
As75
Ag107
Pb208
Bi209
Sb121
Cu65
Zn66 ppm
Cd111 ppm
Co59 ppm
Ni60 ppm
ppm

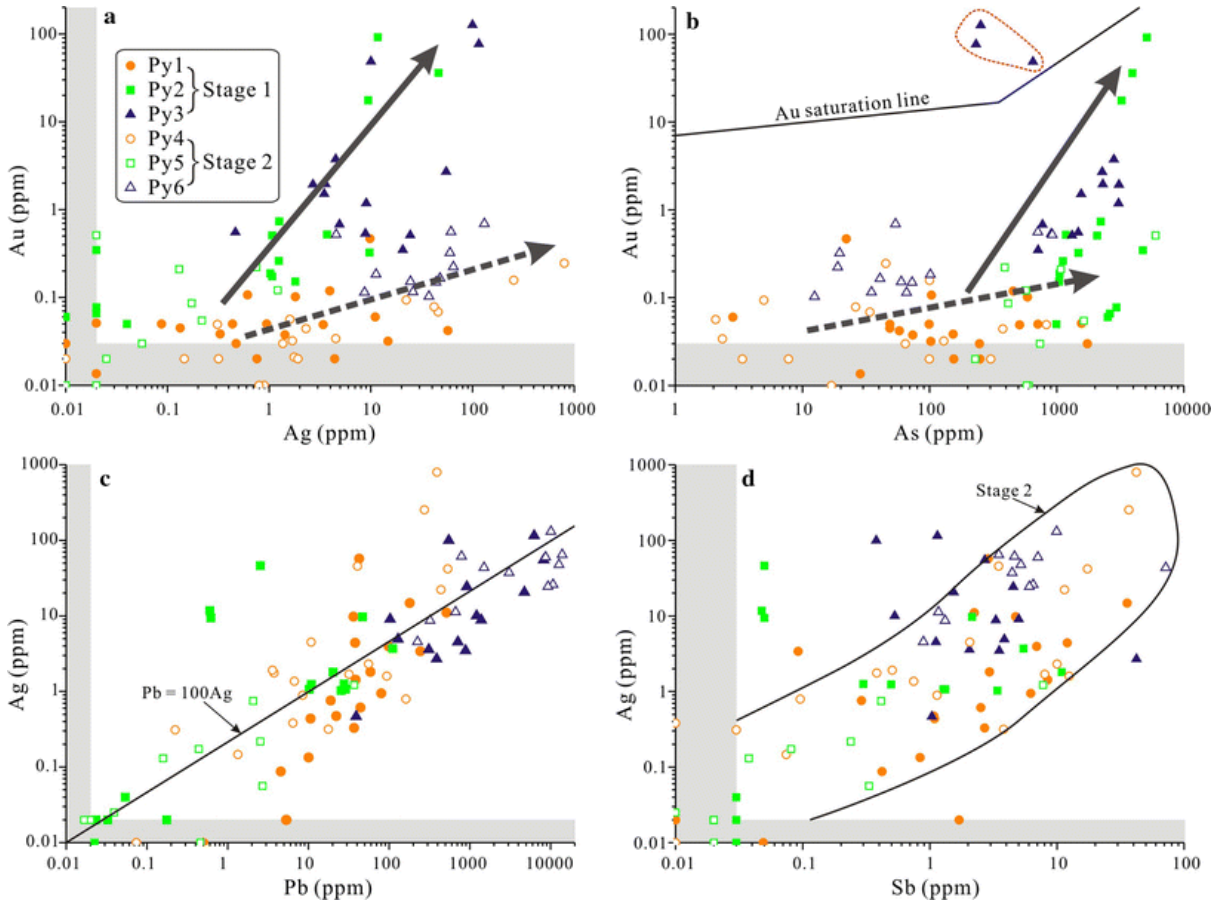
a
Py1
Py2
Py3
Stage 1
Py4
Py5
Py6
Stage 2
Au (ppm)
Ag (ppm)
b
Au saturation line
Au (ppm)
As (ppm)
c
Pb = 100Ag
Ag (ppm)
Pb (ppm)
d
Stage 2
Ag (ppm)
Sb (ppm)

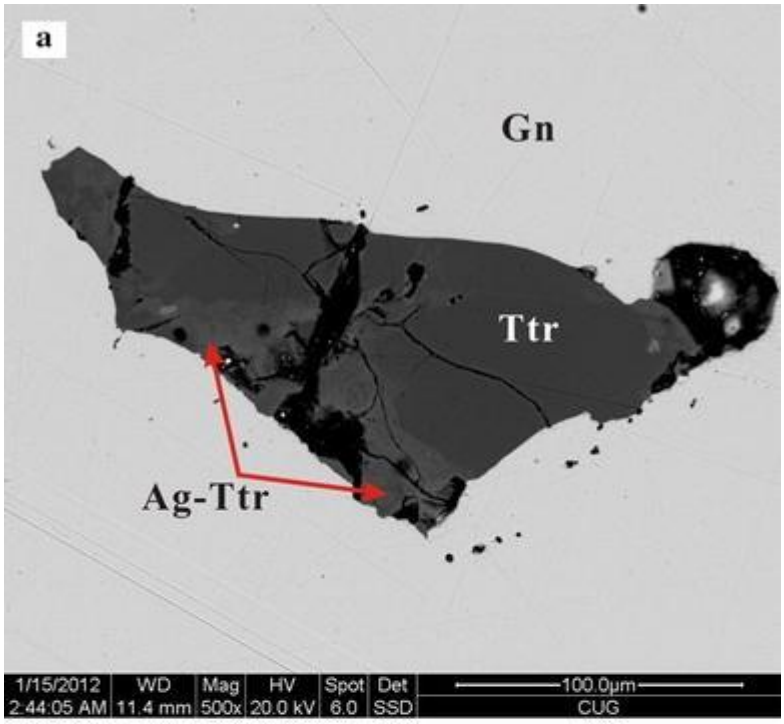
a
Gn
Ttr
Ag-Ttr
1/15/2012 2:44:05 AM
WD 11.4 mm
Mag 500x
HV 20.0 kV
Spot 6.0
Det SSD
100.0µm
CUG

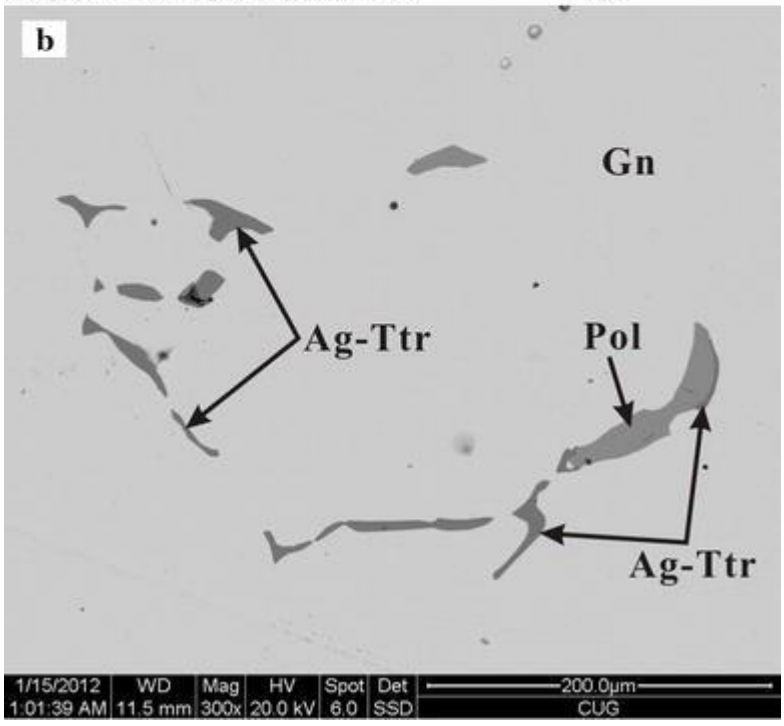
b
Gn
Ag-Ttr
Pol
Ag-Ttr
1/15/2012 1:01:39 AM
WD 11.5 mm
Mag 300x
HV 20.0 kV
Spot 6.0
Det SSD
200.0µm
CUG

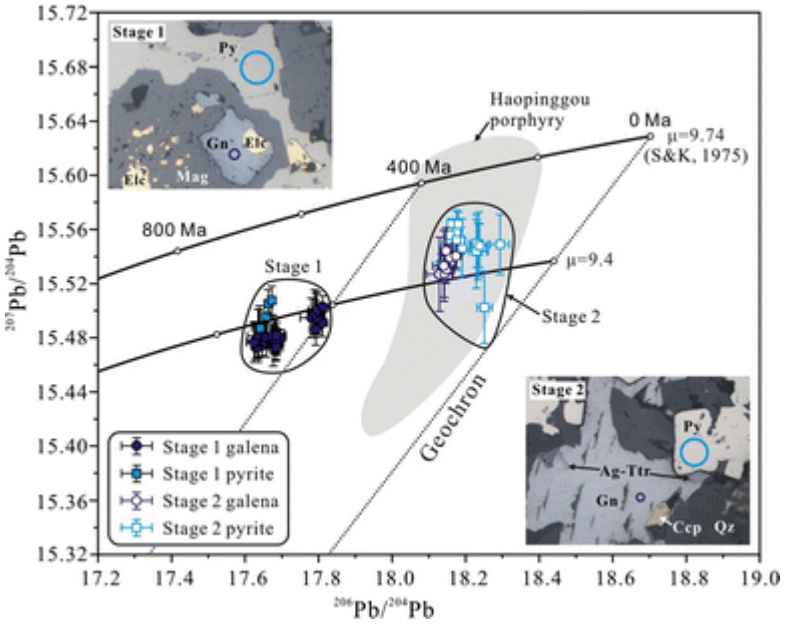
Stage 1
Py
Gn
Ele
Ele
Mag
Haopinggou
porphyry
0 Ma
μ=9.74
(S&K, 1975)
400 Ma
800 Ma
μ=9.4
Stage 1
Stage 2
Geochron
Stage 2
Py
Ag-Ttr
Gn
Ccp
Qz
Stage 1 galena
Stage 1 pyrite
Stage 2 galena
Stage 2 pyrite
15.72
15.68
15.64
15.60
15.56
15.52
15.48
15.44
15.40
15.36
15.32
17.2
17.4
17.6
17.8
18.0
18.2
18.4
18.6
18.8
19.0
$^{207}Pb/^{204}Pb$
$^{206}Pb/^{204}Pb$

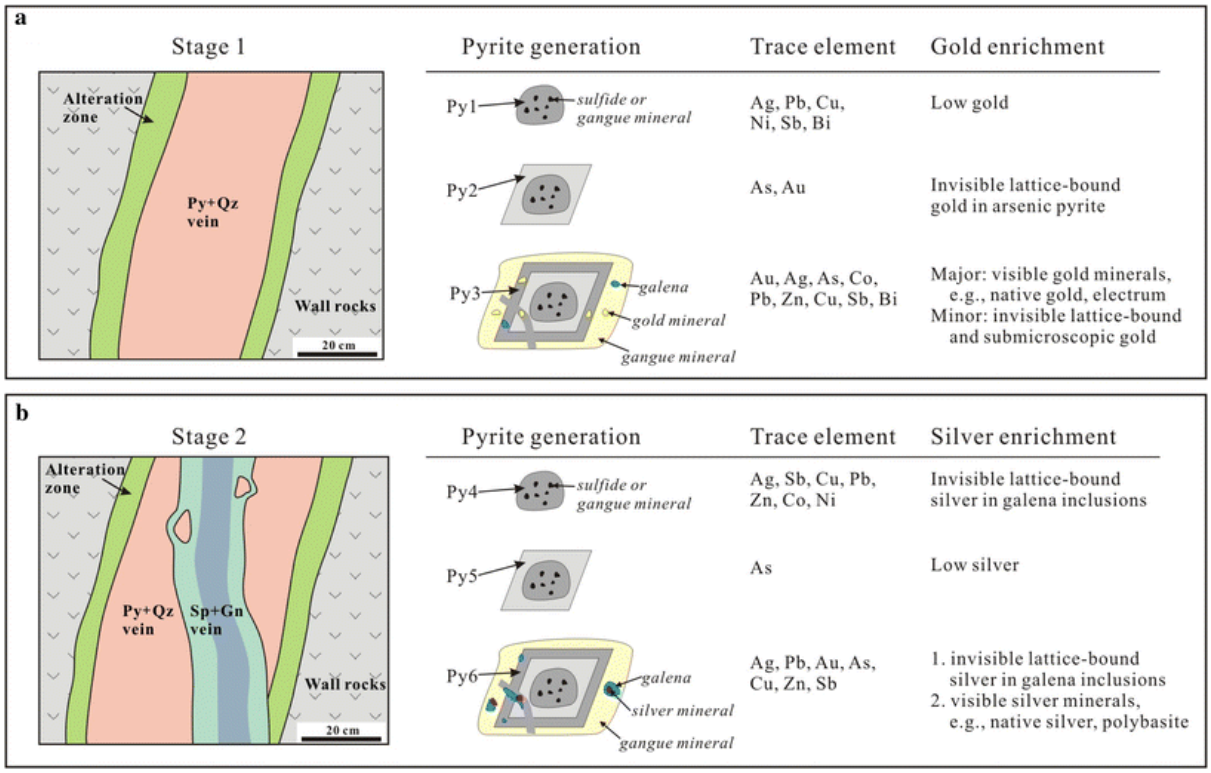
a
Stage 1
Alteration zone
Py+Qz vein
Wall rocks
20 cm
Pyrite generation
Trace element
Gold enrichment
Py1
sulfide or gangue mineral
Ag, Pb, Cu, Ni, Sb, Bi
Low gold
Py2
As, Au
Invisible lattice-bound gold in arsenic pyrite
Py3
galena
gold mineral
gangue mineral
Au, Ag, As, Co, Pb, Zn, Cu, Sb, Bi
Major: visible gold minerals, e.g., native gold, electrum
Minor: invisible lattice-bound and submicroscopic gold
b
Stage 2
Alteration zone
Py+Qz vein
Sp+Gn vein
Wall rocks
20 cm
Pyrite generation
Trace element
Silver enrichment
Py4
sulfide or gangue mineral
Ag, Sb, Cu, Pb, Zn, Co, Ni
Invisible lattice-bound silver in galena inclusions
Py5
As
Low silver
Py6
galena
silver mineral
gangue mineral
Ag, Pb, Au, As, Cu, Zn, Sb
1. invisible lattice-bound silver in galena inclusions
2. visible silver minerals, e.g., native silver, polybasite

Sample no.	Vein no.	Tunnel	Level (m)	Stage	Ore minerals		Gangue minerals	Analyses
					Major	Minor		
HP04	H16	Outcrop	660	Stage 1	Py	Ccp, Gn	Qz	SEM–EDS, LA-ICP-MS
HP32	H16	PD5	610	Stage 1	Py	Ccp, Sp, Elc	Qz, Sd	SEM–EDS, EBSD, LA-ICP-MS
HP41	H16	PD5	610	Stage 1	Py	Ccp, Apy, Gn, Kut	Qz, Sd	SEM–EDS, EBSD, EMP, LA-ICP-MS
HP62	H16	PD5	610	Stage 1	Py, Ccp	Sp, Gn	Qz	SEM–EDS, LA-ICP-MS
HP66	H15	PD3	340	Stage 1	Py	Gn, Ccp, Elc	Qz, Sd, Mag	SEM–EDS, EMP, LA-ICP-MS
HP67	H15	PD3	340	Stage 1	Py	Gn, Po, Au, Elc	Qz, Sd	SEM–EDS, EMP, LA-ICP-MS
HP68	H15	PD3	340	Stage 1	Py	Gn, Sp, Po	Qz, Sd	SEM–EDS, EMP, LA-ICP-MS
HP15	H16	Outcrop	660	Stage 2	Sp, Gn, Py	Ccp, Pol, Prg	Qz	SEM–EDS, EMP
HP42	H16	PD5	610	Stage 2	Sp, Gn, Ccp	Ttr, Pol	Qz, Ank	SEM–EDS, EMP
HP46	H16	PD5	610	Stage 2	Sp, Gn, Py	Ag–Ttr, Pol	Qz	SEM–EDS, LA-ICP-MS
HP47	H16	PD5	610	Stage 2	Sp, Gn, Py	Ag–Ttr, Pol, Arg	Qz	SEM–EDS, LA-ICP-MS
HP63	H16	PD5	610	Stage 2	Sp, Gn	Py, Ttr, Ag–Ttr, Pol	Qz, Ank	SEM–EDS, LA-ICP-MS
HP69	H15	PD2	530	Stage 2	Sp, Gn, Ccp	Py, Cv, Str, Arg	Qz, Ank	SEM–EDS, EMP
HP70	H15	PD2	530	Stage 2	Sp, Gn, Py	Ag–Ttr, Pol, Arg	Qz	SEM–EDS, EMP, LA-ICP-MS
HP79	H17	PD3	470	Stage 2	Sp, Gn, Py	Ccp, Ttr, Ag–Ttr	Qz, Cal	SEM–EDS, LA-ICP-MS
HP81	H17	PD3	470	Stage 2	Sp, Gn, Ttr	Ccp, Pol, Arg, Ag	Qz	SEM–EDS, EMP

Py pyrite, *Sp* sphalerite, *Gn* galena, *Ccp* chalcopyrite, *Po* pyrrhotite, *Au* native gold, *Elc* electrum, *Kut* kustelite, *Cv* covellite, *Ttr* tetrahedrite, *Ag–Ttr* argentiferous tetrahedrite, *Stm* stromeyerite, *Prg* pyrargyrite, *Pol* polybasite, *Arg* argentite, *Ag* native silver, *Qz* quartz, *Mag* magnetite, *Sd* siderite, *Ank* ankerite, *Cal* calcite

Mineral	Analysis no.	Au	As	Ag	S	Fe	Co	Cd	Ni	Sn	Cu	Sb	Zn	Te	Total
Native gold	HP67-1	93.87	b.d.	5.34	0.2	0.22	0.02	0.12	b.d.	0.03	0.15	0.07	0.23	b.d.	100.24
	HP67-2	91.98	b.d.	6.48	0.19	0.24	0.01	0.08	b.d.	0.06	0.19	0.08	0.26	b.d.	99.58
	HP67-3	85.86	b.d.	12.48	0.12	0.31	0.02	0.07	b.d.	0.06	0.13	0.09	0.31	0.04	99.6
Electrum	HP66-1	70.97	b.d.	27.54	0.1	0.42	0.03	0.11	b.d.	0.02	0.14	0.08	0.22	b.d.	99.62
	HP66-2	74.95	b.d.	23.48	0.1	0.21	0.01	0.07	b.d.	0.06	0.13	0.07	0.21	0.04	99.34
	HP66-3	70.6	b.d.	27.57	0.07	0.52	0.03	0.09	b.d.	0.04	0.13	0.06	0.23	b.d.	99.33
	HP66-4	70.51	b.d.	27.88	0.06	0.73	0.02	0.1	b.d.	0.02	0.12	0.03	0.22	b.d.	99.69
	HP66-5	71.21	b.d.	26.9	0.06	0.84	0.01	0.1	b.d.	0.08	0.13	0.09	0.19	0.02	99.63
	HP66-6	69.81	b.d.	27.62	0.06	0.96	0.02	0.09	b.d.	0.04	0.14	0.02	0.21	0.05	99.03
Kustelite	HP41-1	53.78	b.d.	44.48	0.1	0.21	0.03	0.09	b.d.	0.03	0.16	0.01	0.17	0.08	99.14
	HP41-2	49.19	b.d.	50.08	0.1	0.2	0.04	0.08	b.d.	0.01	0.03	0.01	0.15	0.07	99.96
	HP41-3	46.29	b.d.	52.55	0.26	0.26	0.04	0.09	b.d.	b.d.	0.09	0.02	0.21	0.05	99.84
Tetrahedrite	HP42-1-1	0.18	2.68	1.56	25.32	1.26	0.08	0.06	0.16	0.19	37.4	24.69	6.31	b.d.	99.89
	HP42-1-2	0.26	2.22	1.61	25.07	1.3	0.07	0.05	0.16	0.24	37.26	25.45	6.31	b.d.	100
	HP42-2-1	0.26	2.23	1.67	25.62	1.44	0.08	0.06	0.09	0.25	37.01	25.58	6.63	b.d.	100.9
	HP81-1-3	0.23	1.4	6.69	24.4	0.28	0.05	0.06	b.d.	0.21	34.48	25.08	7.05	b.d.	99.92
	HP81-1-4	0.23	1.54	5.58	24.6	0.31	0.04	0.06	b.d.	0.25	35.16	25.24	7.08	b.d.	100.08
	HP81-1-5	0.23	1.39	5.02	24.65	0.33	0.05	0.05	b.d.	0.24	35.19	25.61	7.03	b.d.	99.8
	HP81-2-1	0.23	1.49	5.48	24.56	0.31	0.06	0.05	b.d.	0.23	35.08	25.28	7.03	b.d.	99.79
Argentiferous tetrahedrite	HP70-2-1	0.27	1.74	18.39	23.09	2.2	0.04	0.07	b.d.	0.23	24.34	24.52	4.98	b.d.	99.88
	HP70-2-2	0.28	1.64	19.43	23.2	2.04	0.05	0.06	b.d.	0.21	23.7	24.36	4.88	b.d.	99.84
	HP70-2-3	0.25	1.02	26.28	21.71	2.49	0.05	0.06	b.d.	0.22	18.94	24.69	4.3	b.d.	100.01
	HP70-2-4	0.31	1.71	28.09	21.37	2.8	0.04	0.05	b.d.	0.22	17.83	23.53	4.11	b.d.	100.06
	HP70-1-2	0.29	2.43	19.75	23.12	2.62	0.08	0.06	b.d.	0.18	24.05	22.9	4.84	b.d.	100.32
	HP70-1-3	0.23	2.14	19.75	23.09	2.54	0.05	0.07	b.d.	0.2	23.89	23.38	4.93	b.d.	100.25
Stromeyerite	HP69-2-3	0.21	0.01	28.7	26.45	0.25	0.05	0.05	b.d.	0.05	42.05	0.04	1.68	0.04	99.58
	HP69-2-4	0.18	0.01	32.22	25.57	0.03	0.04	0.06	b.d.	0.03	39.27	0.04	1.57	0.08	99.1
	HP69-3-1	0.32	b.d.	60.1	20.48	0.35	0.03	0.04	b.d.	b.d.	17.35	b.d.	0.5	0.2	99.37
	HP69-3-2	0.26	b.d.	61.62	19.55	0.98	0.03	0.06	b.d.	b.d.	16.56	0.01	0.35	0.19	99.59
	HP69-3-3	0.15	0.03	52.55	19.88	0.31	0.03	0.07	b.d.	b.d.	26.87	0.05	0.17	0.17	100.29
Pyrargyrite	HP15-1-4	0.29	0.03	60.56	16.68	0.12	0.05	0.07	b.d.	0.12	0.43	21.29	0.14	b.d.	99.8
	HP15-1-5	0.26	0.03	59.75	16.52	0.08	0.06	0.06	b.d.	0.12	0.33	22.63	0.12	b.d.	99.95
	HP15-1-6	0.29	0.05	60.4	16.42	0.03	0.06	0.06	b.d.	0.13	0.27	22.27	0.15	b.d.	100.13
	HP15-1-7	0.28	0.01	60.41	16.55	0.08	0.06	0.08	b.d.	0.11	0.34	21.86	0.12	b.d.	99.9
	HP15-1-8	0.28	0.02	60.35	16.18	0.22	0.03	0.05	b.d.	b.d.	0.36	21.67	0.13	0.08	99.35
Polybasite	HP70-1-1	0.25	0.63	73.57	13.43	0.05	0.05	0.06	b.d.	b.d.	3.23	4.96	3.5	0.12	99.85
	HP70-3-1	0.34	0.84	77.06	13.74	b.d.	0.04	0.09	b.d.	b.d.	2.48	5.76	0.16	0.17	100.68
	HP70-3-2	0.32	0.79	75.24	13.6	b.d.	0.07	0.08	b.d.	b.d.	3.39	5.79	0.17	0.16	99.58
	HP70-3-7	0.35	0.62	76.04	13.05	0.02	0.05	0.08	b.d.	b.d.	2.24	7.04	0.4	0.11	99.98
	HP42-2-2	0.3	b.d.	71.32	13.08	0.52	0.05	0.08	b.d.	b.d.	4.22	9.95	0.19	0.08	99.78
Argentite	HP69-2-1	0.33	0.08	79.89	15.23	b.d.	0.03	0.09	b.d.	b.d.	3.17	b.d.	1.18	0.13	100.12
	HP70-3-3	0.26	b.d.	84.34	14.07	b.d.	0.05	0.07	b.d.	b.d.	0.4	0.01	0.14	0.23	99.55
	HP70-3-4	0.27	b.d.	81.18	17.63	b.d.	0.05	0.09	b.d.	b.d.	0.27	b.d.	0.15	0.2	99.84
	HP70-3-6	0.34	0.1	84.04	12.87	b.d.	0.05	0.07	b.d.	b.d.	0.48	0	0.93	0.27	99.14
	HP81-3-1	0.28	b.d.	79.49	16.1	0.48	0.05	0.09	b.d.	b.d.	3.51	0	0.19	0.19	100.37
Native silver	HP81-1-1	0.3	b.d.	97.56	0.67	b.d.	0.06	0.09	b.d.	b.d.	0.5	b.d.	0.46	0.31	99.95
	HP81-1-2	0.32	b.d.	97.99	0.64	b.d.	0.07	0.08	b.d.	b.d.	0.45	b.d.	0.28	0.32	100.15
	HP81-2-2	0.3	b.d.	97.01	0.86	0.28	0.07	0.09	b.d.	b.d.	1.11	0.01	0.27	0.28	100.26
	HP81-2-3	0.27	b.d.	97.06	1.37	0.02	0.06	0.09	b.d.	b.d.	0.69	0.02	0.21	0.34	100.12
	HP81-3-2	0.4	b.d.	97.51	0.82	0.12	0.04	0.11	b.d.	b.d.	0.74	b.d.	0.21	0.34	100.28
	HP81-3-4	0.29	b.d.	97.42	0.64	0.08	0.05	0.1	b.d.	b.d.	0.78	0.02	0.17	0.27	99.82

b.d. below detection